



HAL
open science

Fluid-mediated selective dissolution of subducting carbonaceous material: Implications for carbon recycling and fluid fluxes at forearc depths

Alberto Vitale Brovarone, Simone Tumiati, Francesca Piccoli, Jay J. Ague, James A.D. Connolly, Olivier Beyssac

► To cite this version:

Alberto Vitale Brovarone, Simone Tumiati, Francesca Piccoli, Jay J. Ague, James A.D. Connolly, et al.. Fluid-mediated selective dissolution of subducting carbonaceous material: Implications for carbon recycling and fluid fluxes at forearc depths. *Chemical Geology*, 2020, 549, pp.119682 -. 10.1016/j.chemgeo.2020.119682 . hal-03490156

HAL Id: hal-03490156

<https://hal.science/hal-03490156>

Submitted on 3 Jun 2022

HAL is a multi-disciplinary open access archive for the deposit and dissemination of scientific research documents, whether they are published or not. The documents may come from teaching and research institutions in France or abroad, or from public or private research centers.

L'archive ouverte pluridisciplinaire **HAL**, est destinée au dépôt et à la diffusion de documents scientifiques de niveau recherche, publiés ou non, émanant des établissements d'enseignement et de recherche français ou étrangers, des laboratoires publics ou privés.



Distributed under a Creative Commons Attribution - NonCommercial 4.0 International License

1 **Fluid-mediated selective dissolution of subducting carbonaceous material: implications**
2 **for carbon recycling and fluid fluxes at forearc depths**

3 Alberto VITALE BROVARONE^{1,2*}, Simone TUMIATI³, Francesca PICCOLI⁴, Jay J.
4 AGUE^{5,6}, James A. CONNOLLY⁷, Olivier BEYSSAC¹

5
6 ¹ Institut de Minéralogie, de Physique des Matériaux et de Cosmochimie (IMPMC), Sorbonne Université,
7 Muséum National d'Histoire Naturelle, UMR CNRS 7590, IRD UR206, 75005 Paris, France

8 ² Dipartimento di Scienze della Terra, Università degli Studi di Torino, Via Valperga Caluso 35, 10125 Torino,
9 Italy

10 ³ Dipartimento di Scienze della Terra, Università degli Studi di Milano, via Mangiagalli 34, 20133 Milano, Italy

11 ⁴ Institute of Geological Sciences, University of Bern, 3012 Bern, Switzerland

12 ⁵ Department of Geology and Geophysics, Yale University, New Haven, CT 06520, USA

13 ⁶ Yale Peabody Museum of Natural History, New Haven, CT 06520, USA

14 ⁷ Department of Earth Science, Swiss Federal Institute of Technology, Zurich, Switzerland

15 * Corresponding author: alberto.vitale@unito.it

16

17 **Abstract**

18 Subduction of crustal C governs the long-term global C cycling. The role of carbonates
19 recycling in subduction zones and the related dissolution of C at various depths have been the
20 subject of a large body of literature over the last decades. Much less is known about the
21 contribution of carbonaceous material (CM) to the deep C cycling in subduction zones. This
22 paper presents natural evidence for intense fluid-mediated leaching of CM in pelitic schists at
23 high-pressure/low-temperature conditions relevant to the forearc region of subducting slabs.
24 Manifestations of such process were identified along fluid pathways at various scales in the
25 blueschist-facies subduction complexes of both Alpine Corsica and the Western Alps.
26 Microstructural, whole-rock and Raman analyses across a selected metasomatic aureole were
27 used to quantify the amount and mechanisms of C loss during fluid-rock interaction. In
28 samples affected by intense fluid infiltration, more than 90% of the initial CM was removed
29 from the rock. Microstructural and micro-Raman data indicate selective leaching of
30 disordered CM relative to nearly crystalline graphite. The collected data allowed constraining
31 the magnitude of fluid fluxes required to bleach the studied CM-bearing lithologies at
32 different P-T-fO₂ conditions, which corresponds to rather high time-integrated fluid fluxes in
33 the order of $\sim 10^6$ m³/m². In settings of large-scale fluid channelization, such as along
34 regional-scale, lithological/tectonic boundaries or at the top of the subducted sedimentary
35 pile, intense dissolution of subducted CM is expected. This process may thus exert a negative
36 feedback on the sink of C phases into the deep mantle over the geological timescales and
37 contribute to the release of isotopically light C from subducting slabs in forearc regions.

38

39 **1. Introduction**

40 Subduction of crustal C plays a central role in the global C cycle. Carbonate mineral and
41 carbonaceous material (CM) are the main reservoirs of C in subducting slabs (Hayes and
42 Waldbauer, 2006; Plank, 2014). Metamorphism of carbonate minerals, through either
43 decarbonation/melting reactions or dissolution, has been the focus of considerable research
44 over the last decades (Ague and Nicolescu, 2014; Cook-Kollars et al., 2014; Facq et al., 2014;
45 Gorman et al., 2006; Kelemen and Manning, 2015; Poli, 2015). The contribution of
46 carbonaceous material (CM) to deep C fluxes is less well known, despite the fact that CM is
47 the main input of organic C to subduction zones (Hayes and Waldbauer, 2006; Plank, 2014).
48 With rising temperature during subduction, CM is progressively transformed into graphite
49 through a series of intermediate stages of disordered graphitic C (Buseck and Beyssac, 2014).
50 The progressive transformation of CM into graphite results in loss of heteroatoms such as O,
51 H, and N, as well as some C. Release of C during the earliest transformations of subducted
52 carbonaceous material (< 300 °C) is well established and results in the release of C
53 compounds including thermogenic hydrocarbons and CO₂ (Mullis et al., 1994; Tarantola et
54 al., 2007). At higher metamorphic grades, the behavior of CM is generally considered less
55 mobile than carbonate minerals. Owing to its high buffering potential in oxidized geological
56 fluids (Duncan and Dasgupta, 2017; Hermann et al., 2006), graphitic C, especially crystalline
57 graphite, may be largely retained in the rock even at high temperature conditions. For
58 example, CM is dominantly retained in sedimentary rocks heated by contact metamorphism to
59 temperatures of 600 °C or more (Pattison, 2006). At similar temperature but higher pressure
60 conditions, dissolution of CM is documented during regional Barrovian-style metamorphism
61 of the Wepawaug Schist, Connecticut, USA (Zhang et al., 2018). In this case, a loss of about
62 26% of the bulk rock CM content was observed in kyanite-bearing metapelites (~ 600°C) with
63 respect to lower-grade chlorite-biotite zone precursors. In subduction zones, analysis of
64 sedimentary rocks metamorphosed under closed system conditions suggests that more than
65 75% of the initial subducted CM is preserved down to depths of ~100 km (Cook-Kollars et
66 al., 2014).

67 However, the behavior of subducted CM in open system conditions, e.g. along fluid
68 percolation pathways, is less constrained. Most studies focusing on the behavior of reduced C
69 in open systems have dealt with graphite deposition (Duke and Rumble, 1986; Evans et al.,
70 2002; Galvez et al., 2013; Luque et al., 2009; Vitale Brovarone et al., 2017), whereas fluid-
71 mediated removal of CM is still scarcely documented (Mori et al., 2014). In particular, fluid-
72 rock interactions along channelized fluid pathways may strongly affect the stability of C-
73 bearing phases, as shown for carbonate minerals through processes of decarbonation (Gorman
74 et al., 2006), fluid-mediated carbonate dissolution (Ague and Nicolescu, 2014), or carbonation
75 (Piccoli et al., 2016). Under these circumstances, the conditions suitable for CM mobilization

76 (Tumiati and Malaspina, 2019; Tumiati et al., 2017) may be enhanced relative to closed
77 systems. In particular, although the solubility of CM may be low in aqueous fluids, protracted
78 and/or repeated infiltration of aqueous fluids into CM-bearing lithologies has the potential to
79 progressively remove organic C from the rock.

80 In this contribution, we document natural evidence for fluid-mediated dissolution of CM in
81 metasedimentary rocks at blueschist-facies, high-pressure/low-temperature (HP/LT)
82 conditions within the Schistes Lustrés complex of Alpine Corsica and Western Alps. After a
83 general presentation of the characteristic rocks and microstructures, detailed mineralogical
84 and geochemical data is presented for a selected metasomatic aureole from Alpine Corsica.
85 Microstructural data, bulk CM concentrations, Raman spectroscopy, and thermodynamic
86 calculations are integrated to describe the patterns of fluid rock interactions and dissolution of
87 CM, to estimate the time-integrated fluid fluxes along channelized fluid pathways in the
88 subducting slab at forearc depths, and to examine the related geochemical implications.

89

90 **2. Geologic setting**

91 The Schistes Lustrés complex of Alpine Corsica and Western Alps (Fig. 1) mainly consists of
92 Tethyan oceanic/transitional metaophiolitic rocks and associated metasedimentary cover
93 rocks units that were variably transformed in the Alpine subduction system (Agard et al.,
94 2001; 2002; Beltrando et al., 2010; Elter, 1971; Lagabrielle et al., 2015). In both belts, these
95 units underwent high-pressure/low-temperature (HP/LT) metamorphism ranging from low-
96 grade to lawsonite eclogite-facies conditions (Agard et al., 2009; Angiboust et al., 2009;
97 Fournier et al., 1991; Groppo and Castelli, 2010; Ravna et al., 2010; Schwartz et al., 2013;
98 Vitale Brovarone et al., 2013)).

99 This study centers on the blueschist-facies domain of the Schistes Lustrés complex exposed in
100 Alpine Corsica and Western Alps (Fig. 1). In both belts, this terrane consists mostly of large
101 metasedimentary suites containing variable proportions of CM-rich metapelitic schists and
102 marble layers that incorporate blocks and slices of mafic and ultramafic rocks such as
103 metagabbros, metabasalts, and serpentinites. The juxtaposition of mafic/ultramafic and
104 oceanic sedimentary lithologies are interpreted as the result of pre-subduction gravitational
105 and/or tectonic lithological associations only locally intensely reworked by the Alpine
106 tectonics (Balestro et al., 2015; Lagabrielle et al., 2015; Lagabrielle and Lemoine, 1997;
107 Lemoine, 2003; Polino and Lemoine, 1984; Vitale Brovarone et al., 2014b). These suites are
108 exposed within a rather continuous metamorphic gradient from ~ 300 °C and $P < 1$ GPa to ~
109 480 °C and 1.8 GPa (Agard et al., 2009; Gabalda et al., 2009; Schwartz et al., 2013; Vitale
110 Brovarone et al., 2014b) (Fig. 1b).

111 In the investigated blueschist-facies units, whole rock carbon budgets in metasedimentary
112 rocks unaffected by substantial fluid percolation show a general preservation of the initial
113 marine carbonate and organic C concentrations and C stable isotope signature, pointing to
114 little carbon mobilization during prograde metamorphism (Cartwright and Buick, 2000;
115 Cook-Kollars et al., 2014). In this study we focus on channelized fluid pathways localized
116 along the contacts separating mafic/ultramafic blocks and slices from the enclosing
117 metasedimentary rocks. Previous work has documented the presence of fluid-mediated
118 metasomatic halos along these contacts in the blueschist-facies units of Alpine Corsica. In
119 particular, it has been shown that the metasedimentary rocks in contact with mafic/ultramafic
120 rocks are characterized by the precipitation of metasomatic lawsonite (Vitale Brovarone et al.,
121 2014a; Vitale Brovarone and Beyssac, 2014).

122 Equivalent processes are described in this work for in the equivalent blueschist-facies units of
123 the W. Alps (Fig. 1b). In Alpine Corsica, this phenomenon was observed from minimum T
124 conditions of about 370 °C and corresponding P of ~ 1-1.3 GPa up to the boundary with the
125 underlying eclogite-facies unit at ~ 480 °C and 1.8 GPa (Fig. 1). No evidence for fluid-rock
126 interactions and metasomatism was found within the same lithological suite at lower T in
127 Alpine Corsica, and the T of ~ 370 °C was proposed as a regional-scale isograd for this
128 process (Vitale Brovarone et al., 2014a). In the blueschist units of the Western Alps, evidence
129 for this process was found from slightly lower T conditions of ~ 340 °C (Fig. 1). Owing to the
130 more intense retrograde overprint and lawsonite breakdown in the Western Alps units
131 compared to Alpine Corsica, only overprinted lawsonite metasomatic aureoles were identified
132 at T > 400 °C (Fig. 1).

133

134 **3. Methods**

135 **3.1. Sample collection and preparation**

136 Rock samples were collected in the areas shown in Figure 1, which also presents the
137 distribution of more than 230 outcrops identified in the two belts: > 200 outcrops in Alpine
138 Corsica, part of which was already presented in Vitale Brovarone et al., 2014a, and 32 in the
139 Western Alps (stars refer to main localities). About 80 samples from the two belts were
140 selected for thin section preparation. Fourteen samples were collected from one selected
141 reaction zone in Alpine Corsica (location in Fig. 1a) for detailed geochemical and Raman
142 spectroscopy study. The samples were then cut to remove surface weathering. One chip of
143 approximately 4x4x4 cm was isolated for each sample and cut into two parts for thin section
144 preparation and bulk rock analysis, respectively. For bulk rock analysis, the samples were
145 crushed and then pulverized with an agate mortar.

146

147 **3.2. Bulk-rock C and trace element concentrations**

148 Whole-rock analyses were performed at the Service d'Analyse des Roches et Minéraux
149 (SARM, Centre de Recherches Pétrographiques et Géochimiques, Nancy, France). Total CO₂
150 concentration was analyzed using a LECO SC 144DRPC analyzer (LECO France, Garges les
151 Gonesse, France) through calcination at 1400 °C. The uncertainty on the total CO₂ content is
152 <10% for contents between 0.5 and 1%, <20% for contents between 0.5% and 0.1%, and
153 >20% for contents <0.1% (detection limit 0.01%). Total organic C was analyzed following
154 the same protocol after removal of all carbonates. The uncertainty on the total organic C
155 (Corg) content is <15% for contents between 0.5 and 0.1% and >15% for contents <0.1%
156 (detection limit 0.01%). The bulk inorganic C (carbonate minerals) content in the samples
157 was calculated by subtracting the organic C from the total C. The results are presented in
158 Table 1. The major and trace element analyses were done by alkali fusion of rock samples
159 (LiBO₂), followed by concentration measurements using an ICP-OES Icap 6500
160 (Thermoscientific) for major elements, and an ICP-MS X7 (Thermoscientific) for trace
161 elements (protocol by Carignan et al., 2001). The uncertainty on the elements used for mass
162 balance calculations (see Section 5.2) are Hf: <10%, Th: <10%, and Zr: >5%.

163

164 **3.3. Microscopic observations and Raman spectroscopy**

165 Microstructural and petrographic characterizations were carried out on petrographic thin
166 sections with an optical microscope first, and then by scanning electron microscopy (SEM).
167 Petrographic thin sections were carbon coated for SEM work. Observations were performed
168 at a working distance of 7.5 mm using a Zeiss Ultra 55 field emission gun SEM operated at
169 15 kV with a 120 µm aperture. Backscattered electron (BSE) mode was used to investigate
170 chemical heterogeneities using an Angle Selective Backscattered Detector (AsB) or an
171 Energy Selective Backscattered Detector (EsB).

172 Raman spectra were obtained using a Renishaw InVIA Reflex microspectrometer (IMPMC
173 Paris). We used a 514 nm MODULASER argon laser in circular polarization. The laser was
174 focused on the sample by a DMLM Leica microscope with a 100x objective (NA = 0.85), and
175 the laser power at the sample surface was set around 1 mW. The Rayleigh diffusion was
176 eliminated by edge filters, and to achieve a nearly confocal configuration, the entrance slit
177 was closed down to 15 µm. The signal was finally dispersed using a 1,800 gr/mm grating and
178 analyzed by a Peltier cooled RENCAM CCD detector. Before each session, the spectrometer
179 was calibrated with a silicon standard. Because Raman spectroscopy of CM can be affected
180 by several analytical mismatches, we followed closely the analytical and fitting procedures
181 described by Beyssac et al. (Beyssac et al., 2002; 2003a). Measurements were taken on
182 polished thin sections cut perpendicularly to the main fabrics, and CM was systematically

183 analyzed below a transparent adjacent/including mineral. The spectra were recorded in the
184 extended scanning mode ($700\text{--}2,000\text{ cm}^{-1}$) with acquisition times from 30 to 60 s. The
185 number of spectra for each sample is reported in Figure 3. Spectra were then processed using
186 the software Peakfit using a linear baseline correction and simultaneous peak fitting with a
187 Voigt function (Beysac et al., 2002). The Raman results, expressed as R2 values (see Section
188 4.2 for details), are presented in Table 2.

189

190 **3.4. Thermodynamic modeling**

191 Thermodynamic modeling was used to estimate the solubility of CM at the considered
192 metamorphic conditions and to assess the amount of aqueous fluid required to mobilize CM
193 in the selected samples (Section 5.4). Molar fractions of H_2O , CO_2 and CH_4 in equilibrium
194 with two types of CM for which thermodynamic data are available at the considered
195 metamorphic conditions (Tumiati et al., 2020): an X-ray amorphous, glass-like C (Alpha
196 Aesar, type I; hereafter glass-like C), and crystalline graphite. Based on the thermodynamic
197 data of Tumiati et al. (2020), glass-like C has higher Gibbs free energy compared to graphite
198 at P below around 3 GPa (T playing a minor effect), and consequently higher solubility. For
199 this reason, these two types of CM were considered as reference for higher (glass-like C) and
200 lower (graphite) CM solubility in aqueous fluids at the considered conditions. P–T conditions
201 of 1.0 GPa– 300°C , 1.3 GPa– 370°C and 1.7 GPa– 425°C — consistent with the regional, W-E
202 metamorphic gradient in the considered terranes (Fig. 1) — were considered. The
203 composition of fluids in equilibrium with glass-like C and graphite at the considered
204 conditions have been retrieved using the routine "fluids" of the Perple_X package (Connolly,
205 1995) and the COH fluid EoS by Connolly and Cesare (1993). The CM in the model was
206 considered to be chemically pure, with no heteroatoms such as N, S, and H. For each
207 calculation, the $f\text{O}_2$ was buffered at conditions corresponding to the maximum activity of
208 water (H_2O -maximum hereafter). The calculations were done at C saturation conditions
209 owing to the presence of at least some CM throughout the reaction zones (Section 4.1). A
210 rock density of 2.7 g/cm^3 was considered for the modeled metapelite. The augmented Gibbs
211 free energy of formation of glass-like C has been modeled by setting the activity of C [$a(\text{C})$]
212 in the calculations to values > 1 (Connolly, 1995). The moles of C dissolved in COH fluids, in
213 equilibrium either with graphite or glass-like C, have then been compared with the moles of C
214 leached out from the rocks (averaged to 67.5 mol/m^3 rock, corresponding to 0.03 wt.%
215 graphite, see Section 4.1), yielding the amount of fluid (m^3) required to complete the
216 dissolution process. The calculated fluid compositions are presented in Table 4.

217

218 **4. RESULTS**

219 **4.1. Field and sample description**

220 All collected samples exhibit a marked schistosity parallel to the contact with the
221 mafic/ultramafic blocks. Next to the contact zone, the rocks show a marked bleaching of the
222 metasediments. The thickness of the bleached aureole ranges from a few tens of cm to several
223 meters and systematically matches with the precipitation of lawsonite. As a general feature,
224 the bigger the mafic/ultramafic block, the thicker the metasomatic halo (Vitale Brovarone et
225 al., 2014a). Several examples of these metasomatic rinds can be observed along the road
226 joining Bocca a Serna and Morosaglia in Alpine Corsica (bottom part of the map in Fig. 1a).
227 In the area of Colle dell'Agnello, Western Alps (Fig. 1b), the intersection between
228 metasomatic aureoles rimming large mafic bodies and the topography locally defines large
229 surfaces (tens of m) exposing the lawsonite-bearing, bleached rocks studied here (Fig. 3).

230 The general appearance of the bleached rocks is remarkably similar in the two belts (Figs. 2-
231 4). A characteristic feature of the studied rocks is the presence of dark, CM-rich lawsonite
232 crystals dispersed in a light-colored matrix mainly consisting of lawsonite + quartz + mica ±
233 chlorite (Fig. 4). Rocks showing these features were found only in the proximity of the above-
234 mentioned lithological boundary, or, to a lesser extent, along thin (3-5 cm thick), foliation-
235 parallel veins within the regional metapelitic schists (Fig. 2d-f).

236 In thin section, samples affected by partial bleaching clearly show the preservation of
237 preexisting CM inside the newly formed lawsonite blasts (Fig. 4). For example, Figures 4a
238 and 4e show the preservation of continuous of CM-rich layers of the metapelite inside the
239 lawsonite blasts, and the partial to total bleaching of the same layers outside the blasts. More
240 complex growth microstructures, such as hour-glass zoning highlighted by CM inclusions in
241 the lawsonite blasts (Fig. 4c), are also observed in samples ranging from incipient to
242 enhanced bleaching.

243 For detailed investigations, a ~2.5 m thick metasomatic aureole formed in metapelites in
244 contact with a ~1 km long block of metagabbro was selected in Alpine Corsica (Fig. 5; see
245 Figure 1a for location and Fig. S1 for complementary geological map). This aureole was
246 selected owing to the absence of carbonate layers throughout the reaction zone, the presence
247 of which would have hampered assessing the C budget across the reaction zone. The peak
248 metamorphic conditions for this part of the blueschist-facies unit were estimated at ~420-430
249 °C and 1.6-1.8 GPa based on Raman Spectroscopy on Carbonaceous Material (RSCM) and
250 thermodynamic modeling of CM-bearing metapelites unaffected by fluid-rock interaction
251 (Vitale Brovarone et al., 2014b) (Fig. 1).

252 Across the interaction zone, the metapelite exhibits marked mineralogical variations and a
253 decrease in CM content toward the adjacent metagabbro. Based on the microstructural and
254 mineralogical features and CM content, five zones designed Z1 to Z5, are distinguished,

255 where the number in the designation indicates increasing intensity of metasomatism, i.e.,
256 proximity to the metagabbro. (Figs. 3-6). Zone Z1 (metapelite) mainly consists of white
257 mica, quartz, chlorite, and titanite coexisting with CM, and does not show
258 mineralogical/microstructural evidence for fluid-mediated transformations. The CM content
259 (~0.14 wt.%, Fig. 5) fits the range of metapelitic schists in equivalent metasedimentary suites
260 at comparable metamorphic conditions (Cook-Kollars et al., 2014). For these reasons,
261 samples from Z1 are taken as the reference for charactering the more intensely metasomatized
262 zones.

263 Zones Z2 and Z3 both have a similar mineralogy compared to Z1, except for the fluid-
264 mediated precipitation of large syn-to-post kinematic lawsonite blasts and for different modal
265 proportions (Fig. 5). In Z2, a slight decrease of CM relative to Z1 is observed in the most
266 internal sample, i.e. towards the metagabbro, even though heterogeneous, foliation-parallel
267 bleaching was observed within single thin sections. Carbonaceous material is homogeneously
268 distributed between the matrix and as inclusions in lawsonite and titanite. This feature
269 demonstrates that the CM inclusions in lawsonite represent pre-existing CM rather than fluid-
270 deposited CM. Zones Z2 and Z3 were distinguished because of a sharp decrease in the CM
271 content from Z2 (~0.12 wt.%) to Z3 (~ 0.03 wt.%, Figs. 4, 5), and for slightly higher amounts
272 of quartz in Z3. Zone Z3 titanite and lawsonite blasts are dark and contain abundant
273 inclusions of CM, similar to those in Z2, but the surrounding matrix is lighter in color and
274 contains less CM relative to Z1 and Z2. Moreover, lawsonite in Z3 commonly shows a CM-
275 rich core and a CM-poor/free rim, suggesting that the CM removal happened during the
276 lawsonite precipitation event at high-pressure conditions (Figs. 3, 7d).

277 Zone Z4 mainly consists of quartz and albite (late pseudomorphic product after blue
278 amphibole), together with local mica-chlorite microlithons and corroded titanite and
279 lawsonite. Lawsonite forms large (similar to Z2-Z3) crystals that appear extensively replaced
280 by quartz (Fig. 7f). Nevertheless, a second generation of tiny, idioblastic lawsonite crystals is
281 also observed (Fig. 7f). The CM content of Z4 is below detection limit for bulk measurements
282 (<0.01 wt.%), and is mainly found as inclusions in lawsonite and titanite relicts. Matrix CM in
283 Z4 is very rare and occurs as scattered individual grains.

284 Zone Z5 has a metagabbro-like mineral assemblage (see below for details regarding its
285 metasedimentary origin) and mainly consists of blue amphibole, chlorite and titanite, the
286 titanite being generally inclusion-poor and petrographically different from that in Z1-Z4. The
287 blue amphibole is only partially retrogressed to albite. As in Z4, the CM content of Z5 is
288 below detection limit (<0.01 wt.%).

289 Despite the mineralogical variations in Z4-Z5 compared to Z1-Z3, including the formation
290 and transformation of blue amphibole and partial replacement of lawsonite testifying to a

291 complex metasomatic evolution, the sedimentary origin of the Z4-Z5 rocks is indicated by the
292 rare earth element (REE) patterns. The REE patterns of these rocks are in fact consistent with
293 all other altered and unaltered metapelite-derived zones (Z1-Z3), and clearly differ from the
294 adjacent metagabbro (Fig. S2; Table S1). The metasedimentary origin of Z4-Z5 is also
295 supported by the presence of CM inclusions in titanite (Z5 in Fig. 8). No carbonate was
296 detected by optical and electron microscopy in the studied samples, including in the
297 metagabbro. In one sample, however, the presence of tiny amounts of carbonate is inferred
298 based on the presence of total CO₂ other than CM in the bulk rock analysis (Fig. 5). In the
299 metagabbro, no CM was detected by optical microscopy and the bulk rock CM content is at
300 detection limit (0.01 wt.%) or lower (Table 1). A slight increase of bulk total CO₂ is observed
301 in the metagabbro close to the metasediment, but the bulk concentration remains very low (\leq
302 0.09 wt.%) (Table 1).

303

304 **4.2. Raman spectroscopy of CM across the reaction zone**

305 In order to investigate the patterns and mechanisms of CM removal in the studied samples, a
306 Raman spectroscopy study was carried out to characterize the nature of CM across the
307 reaction zone. The degree of graphitization of CM can be quantified by the relative area of the
308 G, D1, and D2 band of CM in Raman spectra (Fig. 7a-c) (e.g., Beyssac et al., 2002). This is
309 expressed by the D1/(G + D1 + D2) peak area ratio, hereafter referred to as the R2 ratio
310 (Beyssac et al., 2003b); the lower the R2, the more graphitic the CM, with perfectly ordered
311 CM having a R2 value equal to 0 (no defect band) (Fig. 7a-c). For reference, CM heated
312 under regional metamorphic conditions shows the following T-R2 correspondences: 350 °C \approx
313 0.7; 450 °C \approx 0.4; 550 °C \approx 0.2; 650 °C and above \approx 0 (Beyssac et al., 2002).

314 The results of the Raman analysis are presented in Figure 8 and Table 2 as a function of the
315 measured R2 values across the reaction zone. The Raman characterization of CM in this study
316 is aimed at assessing the mode of fluid-CM interaction and removal of bulk CM rather than
317 constraining metamorphic T conditions by RSCM thermometry, which is published elsewhere
318 (Vitale Brovarone et al., 2014b). Nevertheless, for reference, the R2 value of CM in the
319 regional metapelite unaffected by fluid infiltration next to the studied metasomatic aureole
320 typically 0.4-0.6 (Z1 Fig. 8), and corresponds to about 400-450 °C (Fig. 1a).

321 Both CM included in HP minerals such as lawsonite and titanite (CM_{Inc}) and matrix CM
322 (CM_M) were analyzed throughout the reaction zone (Fig. 7d-f, 8). CM_{Inc} in titanite (Z1) and
323 lawsonite (Z2 to Z4) yield rather constant R2 values ranging from 0.4-0.6 (100% of the
324 analyzed CM_{Inc} in Z1; 86% in Z2; 92% in Z3; 100% in Z4). These R2 values match the
325 degree of graphitization of metamorphosed CM observed in non-metasomatized metapelites
326 from the same metamorphic unit. In Z2 and Z3, minor clusters, each < 10% of the analyzed

327 CM_{Inc} , are also present for $R2 < 0.2$, 0.3-0.4, and $\sim 0.6-0.7$ (Fig. 8). Conversely, CM_{Inc} in
328 titanite from Z5 yields a much lower $R2$ cluster < 0.2 (80%) and two subordinate clusters at
329 0.2-0.3 (5%) and 0.3-0.4 (15%). Compared to CM_{Inc} , CM_M shows a progressive decrease
330 from Z1 to Z4. In Z1, CM_M yields values that are reasonably consistent with those for CM_{Inc} ,
331 with $\sim 88\%$ of the analyses clustering at the regional $R2$ range of 0.4-0.6; in addition, $\sim 10\%$
332 of the spot analyses cluster at 0.3-0.4 and $\sim 2\%$ at > 0.2 .

333 In Z2, the regional $R2$ cluster (0.4-0.6) in CM_M decreases to $\sim 68\%$ of the spot analyses, while
334 the 0.3-0.4 cluster increases to $\sim 30\%$. A small cluster > 0.2 ($\sim 2\%$) is also present. In Z3, the
335 regional $R2$ cluster (0.4-0.6) in CM_M further decreases to $\sim 58\%$. The 0.3-0.4 cluster
336 decreases to $\sim 22\%$, and both the > 0.2 cluster and a new cluster at 0.2-0.3 increase to $\sim 9\%$
337 each. In Z4, the regional $R2$ cluster (0.4-0.6) in CM_M drops to $\sim 4\%$ of the spot analyses, the
338 0.3-0.4 cluster further decreases to $\sim 9\%$, whereas the > 0.2 cluster dominates at $\sim 87\%$. No
339 CM_M was found in Z5.

340

341 **4.3. Geochemical variations across the reaction zone**

342 Figure 9 shows a concentration ratio diagram where the composition of samples from Z2 to
343 Z5 (metasomatized rocks) is normalized to the average composition of samples from Z1
344 (protolith rock). Samples of metagabbros close to the contact are normalized to a least altered
345 sample of metagabbro collected at 5.40 m from the contact (sample 29). Across the
346 metapelite-metagabbro contact, K, B, Cs and Rb exhibit a marked depletion in the altered
347 samples relative to the least altered precursor rocks. Lead shows depletion in the metagabbro
348 and an irregular pattern in the metapelite, plausibly representing heterogeneity in bulk sulfide
349 content. Calcium and Sr have similar, yet complex patterns. The metagabbro shows a general
350 depletion in Ca and Sr, except for the most altered sample next to the contact zone. In the
351 metapelite, Ca and Sr initially increase in Z2-Z3 and then decrease in Z4-Z5, but still
352 remaining enriched relative to Z1. In Z5, a decoupling between Ca and Sr is observed, with a
353 slight increase in Ca and a decrease in Sr relative to Z4. Sodium has a different behavior
354 compared to the other considered elements. The altered metagabbro samples show a
355 progressive depletion in Na towards the contact, whereas the opposite trend is observed in the
356 metapelite.

357

358 **5. DISCUSSION**

359 **5.1. Timing and mechanism of fluid-mediated CM dissolution**

360 The systematic decrease bleaching of metasedimentary rocks along lithological boundaries, as
361 well as the detailed microstructural features across the selected metasomatic halo indicate that
362 the observed decrease in CM across the investigated lithological boundary is the result of a

363 fluid-mediated process that happened at HP conditions in the subduction zone. The studied
364 lithological juxtaposition have been interpreted as inherited, oceanic tectonic or sedimentary
365 structures only slightly reworked by the Alpine tectonics (Lagabrielle et al., 2015; Vitale
366 Brovarone et al., 2014b). This indicates that the observed metasomatic features along
367 lithological boundaries formed in response to fluid-mediated processes rather than contact
368 metamorphic (e.g., magmatic injection) processes. Primary variations in the bulk CM content
369 inherited from the protolith rocks may also be present locally but cannot explain the
370 systematic patterns documented along several tens of lithological boundaries of various nature
371 (Figs. 1-5). The detailed characterization of one reaction zone presented in Figures 5-8 clearly
372 indicates that CM was initially present throughout the reaction zone and progressively
373 removed towards the contact with the adjacent metagabbro (see Section 4.1). The preservation
374 of characteristic microstructures of the protolith CM-bearing pelitic schist within the fluid-
375 deposited lawsonite blasts (Fig. 4) also indicates that the CM inclusions in lawsonite represent
376 relicts of the CM initially present in the rock. The Raman analysis additionally confirms that
377 the relict CM preserved as inclusion in lawsonite/titanite across the reaction zone is analogous
378 to the CM of the starting metapelitic rock (Fig. 8). This feature rules out the possibility that
379 the CM inclusions precipitated from the fluid together with the host lawsonite. The observed
380 microstructural patterns of CM depletion in Z3, e.g. CM-rich lawsonite cores and CM-free
381 lawsonite rims, also suggest that the CM leaching happened during the same metasomatic
382 event responsible for the precipitation of lawsonite. This event has been constrained to HP/LT
383 conditions on the basis of distribution along a regional-scale metamorphic isograd (Vitale
384 Brovarone et al., 2014b; 2014a). The initial precipitation of lawsonite in the reaction zone
385 (preserved in Z2-Z4) and associated H₂O increase (Vitale Brovarone and Beyssac, 2014)
386 indicate that the fluid responsible for the removal of CM was dominantly aqueous.

387 The geochemical patterns across the reaction zone provide insights into the driving
388 mechanism for CM leaching. Two alternative hypotheses are discussed: a redox gradient
389 between the two adjacent lithologies in a static fluid, or the infiltration of an external fluid. In
390 the first case, the dominant mechanism of mass transport is diffusion, and a chemical gradient
391 between the metagabbro and the metapelite is expected. Conversely, a more complex pattern
392 potentially including selective mass loss/gain in both lithologies may result from fluid-rock
393 interaction mediated by advection of an external fluid. In the selected metasomatic halo (Fig.
394 5), a chemical gradient controlled by diffusion in a “closed” metasediment-metagabbro
395 system would require some kind of C reprecipitation at the contact between the two
396 lithologies or in the metagabbro, which is not observed (Fig. 6). The general behavior of
397 fluid-mobile elements such as K, Rb, Ba and Cs across the reaction zone is characterized by a
398 marked mass loss on both sides of the contact. Na may suggest a diffusive exchange between

399 the metagabbro and the metapelite (Fig. 9). Nevertheless, the behavior of Na, as well as Ca
400 and Sr, may reflect different fluid-rock equilibration between the fluid and either the
401 metapelite or the metagabbro, perhaps involving some component of mechanical dispersion.
402 Moreover, coupling the Ca and Sr profiles with the observed mineralogical evolution across
403 the contact suggests a protracted fluid-rock reequilibration with initial precipitation (preserved
404 in Z2-Z3) and successive destabilization (Z4-Z5) of lawsonite (see Section 4.1 for details). As
405 a whole, the above evidence suggests a dominantly advective mechanism of mass transport
406 from an external fluid source.

407 The field data also suggest that the externally-derived fluid was primarily channelized parallel
408 to the regional schistosity. Individual samples at the transition from Z2 to Z3 show discrete,
409 foliation-parallel zones of bleaching. Moreover, the individual CM-leached, lawsonite-
410 bearing veins identified within the metasedimentary pile are also parallel to the regional
411 schistosity (Fig. 2c). This feature is in agreement with several previous studies indicating that
412 fluid flow is greatest parallel to lithological boundaries or foliations (Ague, 2014 and
413 references therein).

414 During progressive loss of CM from the rock, the fluid must have been at least transiently
415 enriched in C. Increases in fluid C concentration may have affected the stability of mineral
416 assemblages within the reaction zone. For example, increasing C content in the fluid may
417 favor the breakdown of lawsonite (Nitsch, 1972), which occurred at least transiently in Z4
418 (Section 4.1). The formation of CO₂ may also lower the solubility of SiO₂ in metamorphic
419 fluids (Newton and Manning, 2009), which could explain the increase of quartz modal
420 amount in Z4. Nevertheless, recent experimental studies suggest that CO₂ in graphite-
421 saturated COH systems may strongly increase in the presence of aqueous SiO₂ and the
422 formation of organic complexes (Tiraboschi, 2018; Tumiati et al., 2017). Following these
423 results, the extensive quartz precipitation in Z4 may be ascribed to a process of C dilution in
424 the fluid by either infiltration of aqueous fluids, or the in-situ breakdown of metasomatic
425 lawsonite.

426

427 **5.2. Selective dissolution of subducted disordered CM**

428 Our data indicate that the more disordered CM component of the studied samples was more
429 affected by the fluid infiltration than the crystalline CM. This phenomenon requires
430 consideration of the origin of the two CM types and the related implications for bulk CM
431 dissolution. Based on observations from both present-day sedimentary basins and
432 metamorphic complexes, the CM present in metasedimentary rocks may have three different
433 origins. The first and most common type is the metamorphosed biomass of the protolith
434 sedimentary rock. The second type is the so-called detrital CM, which derives from the

435 erosion of exposed CM-bearing rocks, burned organic material, or any other source of CM-
436 bearing materials. Studies conducted in active sedimentary environments indicate that detrital
437 CM preserved in sediments is typically rather crystalline (low R₂ values) (Bouchez et al.,
438 2010; Galy et al., 2008). The third type is graphitic C deposited by C-saturated fluid (Cesare,
439 1995; Galvez et al., 2013).

440 The Raman analysis across the selected reaction zone indicates the presence of two CM
441 populations being characterized by either disordered CM (high R₂) and nearly crystalline
442 graphite (low R₂) (Fig. 8). The presence of these two populations throughout the reaction
443 zone, including in the metapelite unaffected by fluid-mediated transformations, indicates they
444 were already present in the rock prior to the fluid infiltration. The disordered CM cluster is
445 interpreted to represent metamorphosed biomass, whereas the more crystalline CM cluster
446 most likely represents inherited detrital CM. Other interpretations, such as fluid-deposited
447 graphite, would be incompatible with the observed microstructural, mineralogical, and Raman
448 patterns.

449 Based on the above considerations, the observed patterns of fluid-mediated CM dissolution
450 may be dependent on the initial concentrations of inherited crystalline CM in the rock relative
451 to more disordered CM. Taking Z5 CM as a proxy for the bulk detrital CM content because
452 this zone has no disordered CM left, the bulk concentration of detrital crystalline CM in the
453 original metapelite was < 0.01 wt.% (below detection limit). Because Z4 samples, also
454 containing CM > 0.01 wt.%, are much darker and CM-rich than Z5 (based on optical
455 microscope comparison), it is plausible that the actual concentration of detrital crystalline CM
456 is probably <<0.01 wt.%.

457 Following the method of Ague (1994) and by considering Zr as the least mobile element in
458 this system (Ague, 2017; Zhang et al., 2018), the fractional CM loss across the reaction zone
459 was estimated for each reaction zone relative to Z1 (Table 3). An assumption was made that
460 the initial CM content was similar throughout the reaction zone, as suggested by the
461 comparable microstructural distribution of CM inclusions in lawsonite and titanite from Z2 to
462 Z5.

463 In the most CM-depleted zones the CM concentration is below detection limits, and the mass
464 balance calculations require some assumptions. In these samples, the initial concentration of
465 disordered CM was estimated by considering the proportion of more disordered CM (R₂ >
466 0.2) relative to more crystalline CM (R₂ < 0.2) in the studied samples as deduced by Raman
467 spectroscopy (Fig. 6) with respect to the detection limit (0.01 wt.%). The calculation yielded
468 CM loss of 18% (± 38) in Z2, 84% (± 8) in Z3, > 86% (± 2) in Z4, and > 90% in Z5 (all
469 relative to Z1). The resulting CM mass loss for 100 g of rock relative to Z1 is 0.03 g (± 0.05)
470 in Z2, 0.12 g (± 0.01) in Z3, and >0.12 g and >0.13g in Z4 and Z5, respectively (CM content

471 in Z4–Z5 is below detection limits). The higher uncertainty in the weakly altered Z2 is most
472 probably explained by primary heterogeneities larger than the mass change, and/or the
473 amount of mass change was heterogeneously distributed within Z2. At least the latter
474 hypothesis was observed within a single thin section of Z2, with CM leaching being more
475 pronounced along discrete foliation-parallel layers (Fig. 5). For comparison, fractional CM
476 loss across the reaction zone was also calculated considering Hf and Th as the least-mobile
477 elements and yielded very similar results to Zr (Table 3). The calculations are actually fairly
478 insensitive to the reference element chosen for Z3–Z5 because the percentages losses of CM
479 are so large.

480

481 **5.3. Fluid-rock regime of CM dissolution**

482 As previously observed in sedimentary environments (Bouchez et al., 2010; Galy et al., 2008)
483 and predicted for metamorphism (Connolly, 1995; Ziegenbein and Johannes, 1980), the
484 response of CM to fluid-rock interactions may be different depending upon its degree of
485 graphitization (Souche et al., 2012). From a thermodynamic point of view, disordered CM is a
486 metastable phase during metamorphism, and a fluid in metastable equilibrium with such
487 material is theoretically enriched in C compared to pure/crystalline graphite (Ziegenbein and
488 Johannes, 1980) (Tumiati et al., 2020). Flushing of this material by aqueous fluids and
489 protracted fluid-rock equilibration is therefore expected to selectively remove disordered CM
490 from the rock with respect to a more crystalline CM, and our Raman spectroscopy dataset
491 confirms this theoretical assumption. Nevertheless, the widespread preservation of disordered
492 CM in the regional metapelitic rocks unaffected by strong fluid-rock interaction indicates that
493 this expectation becomes relevant only in the case of major fluid infiltration; the
494 approximation of CM to pure graphite for thermodynamic calculations appears to be
495 reasonable in closed systems.

496 Equilibria between fluids and CM have been classically described in the COH system
497 (Connolly, 1995; Holloway, 1984). In this system, any fluid in equilibrium with CM is
498 expected to lie on a metastable CM-saturation curve. The position of the curve is dependent
499 on the P and T conditions, and on the crystallinity of the CM (Ziegenbein and Johannes,
500 1980). The concentration of C in a graphite-saturated COH fluid in equilibrium with CM
501 increases with increasing T, with decreasing P, and/or with decreasing crystallinity of the
502 CM. An increase in CM crystallinity, in the case of subduction metamorphism, would also
503 require an increase in T.

504 Therefore, the observed CM leaching could be explained by an infiltrating fluid migrating
505 along either an up-T or a down-P gradient. Up-T fluid circulation has been proposed in the
506 metamorphic units of Alpine Corsica, but within inherited fractures unrelated to the regional

507 foliation (Vitale Brovarone et al., 2018b). In the present case, field relationships suggest that
508 the fluid flow was dominantly foliation-parallel, which in a simple slab thermomechanical
509 configuration would correspond to a slab-parallel, down-T flow. However, because a down-T,
510 down-P flow would lead to C precipitation rather than leaching (Cesare, 1995), an up-dip
511 fluid flux along a rather constant T (i.e., along a slab parallel geotherm) is the most likely
512 condition to dissolve C at the considered conditions.

513 Alternatively, or complementary to an isothermal up-dipgradient, another mechanism can be
514 proposed based on the recent experimental and thermodynamic results by Tumiati et al.
515 (2017). The authors showed that the C concentration in a graphite or, more generally, CM-
516 bearing system can vary by 30% in the presence of dissolved SiO₂ relative to a pure COH
517 system, and without significant variations in f_{O_2} . This was explained by the formation of
518 organosilicon complexes in the fluid (Tumiati et al., 2017). The complex evolution of the
519 studied metasomatic aureole preserved from Z2 to Z5 clearly documents fluid-rock variations
520 involving initial lawsonite precipitation (preserved in Z2) and successive consumption (Z3-
521 Z5). The precipitation of abundant quartz in Z3-Z5 demonstrates aqueous SiO₂ oversaturated
522 conditions that could have favored the extreme CM depletion in the same zones. We therefore
523 propose that the mechanism of fluid-mediated CM removal was driven by either a down-P
524 gradient, or by modifications of the dissolved SiO₂ in the fluid-rock system, or a combination
525 of them.

526

527 **5.4. Fluid fluxes responsible for selective CM dissolution**

528 The removal of disordered CM relative to the more crystalline CM allows assessment of the
529 aqueous fluid fluxes required to achieve the observed CM removal in the field area. Flux
530 estimates were calculated based on the predicted C solubility in fluids in equilibrium with
531 either crystalline graphite (lower solubility) and glass-like C (higher solubility) (Tumiati et
532 al., 2020; see section 3.4 for details). Glass-like C is not expected to be present in natural
533 samples of metamorphic rocks but is considered here as a low solubility reference compared
534 to graphite based on the available thermodynamic data at the considered P-T conditions
535 (Tumiati et al. 2020). Under the assumption that the studied CM was chemically pure (see
536 Section 3.4), the observed selective removal of disordered CM indicates that this phase was
537 metastable relative graphite. This would imply that the disordered CM was more soluble than
538 graphite. However, because thermodynamic data for the disordered CM present in the natural
539 samples are not available, the higher or lower solubility of this material relative to the glass-
540 like C used by Tumiati et al. (2020) cannot be assessed. The range of CM solubility
541 considered in this study therefore provides a qualitative constrain on the magnitude of

542 aqueous fluid infiltration responsible for the selective removal of disordered CM relative to
543 more crystalline CM.

544 Calculations at H₂O-maximum conditions were done at three different sets of P and T
545 conditions: 300 °C and 1 GPa, 370 °C and 1.3 GPa, and 425 °C and 1.7 GPa. These
546 correspond to low-T prograde conditions, the regional isograd of lawsonite metasomatism and
547 associated CM leaching, and the peak metamorphic conditions of the selected samples,
548 respectively (Section 3.4). Based on the thermodynamic model of Tumiati et al. (2020), the
549 solubility of glass-like C is 23% higher than graphite at 300 °C/1 GPa, 21% higher at 370
550 °C/1.7 GPa, and 18% higher at 425 °C and 1.7 GPa.

551 As introduced above, the disordered CM component present in the studied rocks is expected
552 to be less soluble than glass-like C, and more soluble than graphite. The following discussion
553 is therefore not intended to be quantitative on the amount of fluid flux, but rather to assess the
554 patterns of selective leaching of disordered CM (this section) and the magnitude of fluid flux
555 (Section 5.5).

556 Table 4 shows the calculated cumulative volumes of H₂O required to mobilize either graphite
557 or glass-like C according to the calculated fractional mass losses per m³ of rock (Section 5.2).
558 The resulting water:rock ratio area also shown (Table 4). For a given *f*O₂ buffer such as the
559 H₂O-maximum, these ratios are conservative as only the fraction of fluid required to mobilize
560 the CM was considered. As water:rock ratios provide only partial information on the
561 mechanisms of fluid/rock interaction, the time-integrated fluid fluxes (Ague, 2014;
562 Baumgartner and Ferry, 1991) required to achieve the observed CM losses were estimated
563 across the reaction zone as discussed in Section 3.3.

564 Time-integrated fluid fluxes (q_{TI}) are calculated with equation 21 in Ague (1998) that is valid
565 for advection dominated systems with small porosity ($\phi < 0.01$):

566
$$q_{TI} = L_{GF} \frac{m_i}{(C_i^{eq} - C_{i,x=0}^{input})}$$

567 Where L_{GF} is the distance of the geochemical front propagation, m_i is the number of moles of
568 *carbon* consumed per unit volume (mol m⁻³) estimated from mass balance analysis, C_i^{eq} is the
569 fluid composition that would be in equilibrium with the mineral assemblage, and $C_{i,x=0}^{input}$ is the
570 initial fluid composition. C_i^{eq} corresponds to the experimentally determined solubility of
571 either glass-like C or graphite (Tumiati et al, 2020), whereas $C_{i,x=0}^{input}$ is set to zero in order to
572 have the most conservative results. Results are presented in Table 5.

573 The results, shown in Figure 10, are dependent on the distance of reaction front propagation
574 (L), which corresponds to the distance of fluid percolation parallel to the lithological
575 boundary. The parameter n on the vertical axis is the log₁₀ of L expressed in meters. For
576 example, for L = 10 m, n = 1.

577 Three general patterns are observed: (i) the time-integrated fluid fluxes (q_{TI}) required to
578 achieve the observed CM losses decrease with increasing T and P, in agreement with the
579 general behavior of the COH system at C-saturated conditions (Connolly, 1995; Holloway,
580 1984); (ii) at a given P-T condition, the flux is higher for graphite relative to glass-like C, in
581 agreement with earlier studies (Ziegenbein and Johannes, 1980); and (iii) the Δq_{TI} between
582 graphite and glass-like C ($\Delta q_{TI_{\text{graphite-glass-like C}}}$) decreases with increasing P (and T to a lesser
583 degree, Tumiati et al., 2020). More specifically, the $\Delta q_{TI_{\text{graphite-glass-like C}}}$ is of the order of $1.8 \cdot$
584 $10^n \text{ m}^3/\text{m}^2$ at 300 °C and 1 GPa, $0.8 \cdot 10^n \text{ m}^3/\text{m}^2$ at 370 °C and 1.3 GPa, and $0.5 \cdot 10^n \text{ m}^3/\text{m}^2$ at
585 425 °C and 1.7 GPa.

586 The profiles in Figure 10 also indicate that the fluid flux was higher close to the lithological
587 boundary and progressively decreased towards the metasedimentary rocks in a way consistent
588 with the numerical simulations of Ague (2007) for fluid flow in mélangé systems. Variations
589 in the size and geometry of the reaction zone and magnitude of fluid flux are expected
590 depending on the size and shape of the blocks (Ague, 2007).

591 The above calculations show that degree of CM crystallinity has a lower effect on the
592 selective dissolution of disordered CM at P-T conditions of 1.7 GPa and 425°C (peak
593 conditions for the selected aureole) relative to lower-grade conditions (Fig. 10). The field
594 isograd for the companion lawsonite metasomatism and CM leaching suggests that this fluid-
595 mediated process took place at conditions of ~ 370 °C and ~ 1.3 GPa in Alpine Corsica. At
596 these conditions, the $\Delta q_{TI_{\text{graphite-glass-like C}}}$ is slightly higher compared to peak conditions (Fig.
597 10). We therefore suggest that the selective leaching was achieved during the prograde path of
598 the selected rocks where the difference in solubility between disordered CM and graphite was
599 higher. In the Western Alps, evidence for CM leaching in equivalent lithological contexts was
600 observed at lower T in the range of 340 °C (Fig. 1), suggesting slightly different regional fluid
601 flow patterns, but likely similar orders of magnitude compared to Corsica, as discussed in the
602 next section.

603

604 **5.5. Insights on the magnitude of intra-slab fluid flow along lithological boundaries**

605 The above mass balances provide information on the magnitude of fluid flux channelized
606 along lithological boundaries under blueschist-facies conditions in subduction zones.
607 Although the flux estimates presented in the previous section refer to the CM loss measured
608 in one metamorphic alteration profile, the general patterns of CM leaching observed at the
609 regional scale in Alpine Corsica and Western Alps equivalents plausibly suggest comparable
610 orders of magnitude. Considering the exposed length of the metasediment-metagabbro contact
611 (~ 1 km) as a value for L, the time-integrated fluid fluxes would increase by three orders of
612 magnitude compared to the values reported in Figure 9 (i.e., $n = 3$) and reach values as high as

613 $10^6 \text{ m}^3/\text{m}^2$ in Z5 (~0.8 m in thickness). This clearly indicates conditions of channelized fluid
614 flow along conduits (see Ague, 2014 for comparison with flux estimates in various crustal
615 settings). The dependency of the time-integrated fluid flux on the length of the reaction front
616 is also consistent with the observation that the thickness of the reaction zone is qualitatively
617 correlated with the size of the mafic/ultramafic block (Vitale Brovarone et al., 2014a).
618 Moreover, because of permeability contrast, the largest fluxes will be concentrated around the
619 margins of the largest blocks (Ague, 2007).

620

621 Figure 11 qualitatively describes the fluid flux distribution in the investigated block-in matrix
622 lithological suite, at different depths. The same concept can apply to tectonic mélange
623 complexes (Ague, 2007). For example, evidence for CM leaching in metasedimentary rocks is
624 reported in an ultramafic mélange in Japan (Mori et al., 2014). Even though the order of
625 magnitude of the time-integrated fluid fluxes is similar at the three chosen P-T conditions,
626 according to Figure 10, it is expected that the fluid fluxes along lithological boundaries
627 progressively decrease with depth.

628 The distribution of the observed fluid-mediated processes along lithological boundaries or as
629 individual channels (both parallel to the regional foliation) suggests that potentially large
630 amounts of subduction zone fluids can migrate up-slab, thus limiting the amount of fluid
631 transferred to the mantle wedge (Angiboust et al., 2014; Piccoli et al., 2016; Wilson et al.,
632 2014).

633

634 **5.6. Role of fluid-mediated dissolution of graphitic C to subduction C fluxes**

635 Subducted CM is generally considered to be largely retained in the rock during prograde
636 metamorphism, as indicated by regional-scale analysis of metamorphosed oceanic sediments
637 in orogenic belts (Cook-Kollars et al., 2014). However, experimental results indicate that CM,
638 including crystalline graphite, is indeed soluble in aqueous fluids at metamorphic conditions
639 (Tumiati et al., 2017; 2020), making it susceptible to fluid-mediated mobilization along
640 permeability channels. Our study confirms that subducted CM can be mobilized along
641 channelized fluid pathways at forearc conditions. Although our results support a general
642 preservation of highly crystalline CM at P and T conditions not exceeding 1.7 GPa and
643 425°C , only slight variations relative to the estimated fluxes would result in removal of
644 crystalline graphite. It is not excluded, at least in Z5 of the studied natural profile, that some
645 of the more graphitic CM was actually removed from the rock. In any case, the fluid-mediated
646 dissolution of CM documented in this study, as well as the experimental data by Tumiati et al.
647 (2020), suggests that a region of potential release of significant amounts of C through fluid-
648 mediated mobilization of disordered CM may exist in subduction zones. Mass balance

649 analysis shows that nearly complete removal of CM can happen in metapelitic rocks adjacent
650 to lithological boundaries channelizing aqueous fluids (Table 3). Field relationships and
651 numerical models indicate that the thickness of bleached zones is function of the length of the
652 lithological boundary, or, in other words, the length of the fluid channel (Ague, 2007). In the
653 present case studies. Prograde infiltration of aqueous fluids through rocks containing
654 disordered CM may therefore exert a negative feedback on the sink of refractory C-bearing
655 phases into the mantle by subtracting a fraction of the subducted organic C from the rock
656 prior to full graphitization.

657 The significance of this process on global carbon fluxes would depend on the extent and
658 distribution of metasediment-hosted fluid channels. The studied field areas suggest that these
659 channels can be very common within lithologically heterogeneous metamorphic units (Fig. 1),
660 such as subducted sedimentary mélanges or plate-interface tectonic mixings. Similarly, fluid
661 channelized along the top of the subducting slab, or along the base of the slab sedimentary
662 rocks, has potential to mobilize significant amounts of reduced C. Flushing of metapelitic
663 rocks by graphite-undersaturated reduced aqueous fluids, for example generated by hydration
664 (Vitale Brovarone et al., 2017) or dehydration (Piccoli et al., 2019) of ultramafic rocks in the
665 subduction zone, may enhance the dissolution of CM relative to more oxidized fluids
666 (Connolly, 1995). In the absence of significant carbonate minerals, dissolution of CM may
667 impart a light $\delta^{13}\text{C}$ signature to the slab-derived fluids transferred to shallower reservoirs.
668 Considering the $\delta^{13}\text{C}$ signature of CM at the relevant metamorphic conditions in carbonate
669 free metasediments of $\sim -25\text{‰}$ (Cook-Kollars et al., 2014), and the fluid speciation of
670 graphite-saturated systems at the H_2O -maximum, the fluid generated by the CM dissolution
671 would have $\delta^{13}\text{C}$ of $\sim -25\text{‰}$ and -23‰ at 300 °C and 425 °C, respectively (graphite- CO_2 and
672 graphite- CH_4 fractionation factors from Bottinga et al 1969). If the process of CM dissolution
673 happens through infiltration of graphite-undersaturated reduced fluids, the resulting fluids
674 would be even lighter. A possible natural example of generation and circulation of such fluids
675 are documented by Spandler et al. (2008), who reported isotopically light, fluid-deposited
676 carbonate (as low as -12‰) in metasomatized sequences from the metamorphic belt of New
677 Caledonia. In the same terrane, metasedimentary rocks are CM-depleted compared to
678 equivalent sequences unaffected by intense fluid circulation (Vitale Brovarone et al., 2018a).

679

680 **6. CONCLUSIONS**

681 We collected field, microstructural, geochemical, and thermodynamic data showing that
682 channelized, fluid-mediated dissolution of CM can be an efficient process at forearc depth in
683 subducting slabs. Our study shows that, within individual samples, the removal of CM was
684 more efficient for disordered CM relative to crystalline CM, providing a means to constrain

685 the magnitude of fluid fluxes at different depths within the subducting slab. The data collected
686 herein indicate that the order of magnitude of fluid fluxes along channelized pathways at
687 blueschist-to-eclogite-facies conditions is large enough to potentially remove the entire
688 amount of organic C from a given volume of rock, but only in the presence of channelized
689 fluid flow. The widespread distribution of fluid-mediated removal of CM along lithological
690 boundaries in two investigated mountain belts indicates that the estimated magnitude of
691 channelized fluid-fluxes can be common in the forearc regions of subduction zones where
692 subducted CM is structurally disordered. This fluid-mediated process is expected to mobilize
693 significant amounts of isotopically light, reduced C along the top of the slab or at the base of
694 the subducted sedimentary crust.

695 **Acknowledgements**

696 We would like to thank Balz Kamber for editorial handling and two anonymous reviewers for
697 their comments on our study. This work benefited from financial support by LabEx Matisse,
698 ANR-T ERC, MIUR Levi Montalcini program, CNRS - INSU (Syster program), and
699 Emergence de la ville de Paris program. Support by the Deep Carbon Observatory (DCO) is
700 also acknowledged. Scanning Electron Microscope (SEM) facility of the Institut de
701 Minéralogie, de Physique des Matériaux et de Cosmochimie is supported by Région Ile de
702 France grant SESAME 2006 N_ I-07-593/R, INSU-CNRS, INP-CNRS, University Pierre et
703 Marie Curie – Paris 6, and by the French National Research Agency (ANR) grant no. ANR-
704 07-BLAN-0124-01.

705

706 **REFERENCES**

- 707 Agard, P., Jolivet, L., Goffé, B., 2001. Tectonometamorphic evolution of the Schistes Lustrés
708 complex: implications for the exhumation of HP and UHP rocks in the Western Alps.
709 Agard, P., Monié, P., Jolivet, L., Goffé, B., 2002. Exhumation of the Schistes Lustrés
710 complex: in situ laser probe $^{40}\text{Ar}/^{39}\text{Ar}$ constraints and implications for the Western Alps.
711 *Journal of metamorphic Geology* 20, 599–618. doi:10.1046/j.1525-1314.2002.00391.x
712 Agard, P., Yamato, P., Jolivet, L., Burov, E., 2009. Exhumation of oceanic blueschists and
713 eclogites in subduction zones: Timing and mechanisms. *Earth Science Reviews* 92, 53–
714 79. doi:10.1016/j.earscirev.2008.11.002
715 Ague, J.J., 2017. Element mobility during regional metamorphism in crustal and subduction
716 zone environments with a focus on the rare earth elements (REE). *American Mineralogist*
717 102, 1796–1821. doi:10.2138/am-2017-6130
718 Ague, J.J., 2014. Fluid Flow in the Deep Crust, in: *Treatise on Geochemistry*. Geological
719 Society of America, pp. 203–247. doi:10.1016/B978-0-08-095975-7.00306-5
720 Ague, J.J., 2007. Models of permeability contrasts in subduction zone mélange: Implications
721 for gradients in fluid fluxes, Syros and Tinos Islands, Greece. *Chemical Geology* 239,
722 217–227. doi:10.1016/j.chemgeo.2006.08.012
723 Ague, J.J., Nicolescu, S., 2014. Carbon dioxide released from subduction zones by fluid-
724 mediated reactions. *Nature Geoscience* 7, 355–360. doi:10.1038/ngeo2143
725 Angiboust, S., Agard, P., Jolivet, L., Beyssac, O., 2009. The Zermatt-Saas ophiolite: the
726 largest (60-km wide) and deepest (c.70-80 km) continuous slice of oceanic lithosphere
727 detached from a subduction zone? *Terra Nova* 21, 171–180. doi:10.1111/j.1365-
728 3121.2009.00870.x

- 729 Angiboust, S., Pettke, T., De Hoog, J.C.M., Caron, B., Oncken, O., 2014. Channelized Fluid
730 Flow and Eclogite-facies Metasomatism along the Subduction Shear Zone. *Journal of*
731 *Petrology* 55, 883–916. doi:10.1093/petrology/egu010
- 732 Balestro, G., Festa, A., Tartarotti, P., 2015. Tectonic significance of different block-in-matrix
733 structures in exhumed convergent plate margins: examples from oceanic and continental
734 HP rocks in Inner Western Alps (northwest Italy). *International Geology Review* 57,
735 581–605. doi:10.1080/00206814.2014.943307
- 736 Baumgartner, L.P., Ferry, J.M., 1991. A model for coupled fluid-flow and mixed-volatile
737 mineral reactions with applications to regional metamorphism. *Contributions to*
738 *Mineralogy and Petrology* 106, 270–285.
- 739 Beltrando, M., Lister, G.S., Rosenbaum, G., Richards, S., Forster, M.A., 2010. Recognizing
740 episodic lithospheric thinning along a convergent plate margin: The example of the Early
741 Oligocene Alps. *Earth Science Reviews* 103, 81–98. doi:10.1016/j.earscirev.2010.09.001
- 742 Beyssac, O., Goffé, B., Chopin, C., Rouzaud, J.-N., 2002. Raman spectra of carbonaceous
743 material in metasediments: a new geothermometer, *Journal of Metamorphic Geology*.
- 744 Beyssac, O., Goffé, B., Petitet, J.-P., Froigneux, E., Moreau, M., Rouzaud, J.-N., 2003a. On
745 the characterization of disordered and heterogeneous carbonaceous materials by Raman
746 spectroscopy. *Spectrochimica Acta Part A: Molecular and Biomolecular Spectroscopy* 59,
747 2267–2276. doi:10.1016/S1386-1425(03)00070-2
- 748 Beyssac, O., Goffé, B., Petitet, J.-P., Froigneux, E., Moreau, M., Rouzaud, J.-N., 2003b. On
749 the characterization of disordered and heterogeneous carbonaceous materials by Raman
750 spectroscopy. *Spectrochimica Acta Part A: Molecular and Biomolecular Spectroscopy* 59,
751 2267–2276. doi:10.1016/S1386-1425(03)00070-2
- 752 Bouchez, J., Beyssac, O., Galy, V., Gaillardet, J., France-Lanord, C., Maurice, L., Moreira-
753 Turcq, P., 2010. Oxidation of petrogenic organic carbon in the Amazon floodplain as a
754 source of atmospheric CO₂. *Geology* 38, 255–258. doi:10.1130/G30608.1
- 755 Buseck, P.R., Beyssac, O., 2014. From Organic Matter to Graphite: Graphitization. *Elements*
756 10, 421–426. doi:10.2113/gselements.10.6.421
- 757 Cartwright, I., Buick, I.S., 2000. Fluid generation, vein formation and the degree of fluid–
758 rock interaction during decompression of high-pressure terranes: the Schistes Lustrés,
759 Alpine Corsica, France. *Journal of metamorphic Geology* 18, 607–624.
760 doi:10.1046/j.1525-1314.2000.00280.x
- 761 Cesare, B., 1995. Graphite precipitation in C-O-H fluid inclusions: closed system
762 compositional density changes, and thermobarometric implications. *Contributions to*
763 *Mineralogy and Petrology* 122, 25–33.
- 764 Connolly, J.A.D., 1995. Phase diagram methods for graphitic rocks and application to the
765 system C–O–H–FeO–TiO₂–SiO₂. *Contributions to Mineralogy and Petrology* 119, 94–
766 116.
- 767 Connolly, J.A.D., Cesare, B., 1993. C-O-H-S fluid composition and oxygen fugacity in
768 graphitic metapelites. *Journal of metamorphic Geology* 11, 379–388.
- 769 Cook-Kollars, J., Bebout, G.E., Collins, N.C., Angiboust, S., Agard, P., 2014. Subduction
770 zone metamorphic pathway for deep carbon cycling: I. Evidence from HP/UHP
771 metasedimentary rocks, Italian Alps. *Chemical Geology* 386, 31–48.
772 doi:10.1016/j.chemgeo.2014.07.013
- 773 Duke, E.F., Rumble, D., 1986. Textural and isotopic variations in graphite from plutonic
774 rocks, South-Central New Hampshire. *Contributions to Mineralogy and Petrology* 93,
775 409–419. doi:10.1007/BF00371711
- 776 Duncan, M.S., Dasgupta, R., 2017. Rise of Earth's atmospheric oxygen controlled by efficient
777 subduction of organic carbon. *Nature Geoscience* 10, 387–392. doi:10.1038/ngeo2939
- 778 Elter, G., 1971. Schistes lustrés et ophiolites de la zone piémontaise entre Orco et Doire
779 Baltée (Alpes Graies). Hypothèses sur l'origine des ophiolites. *Géologie Alpine* 47, 147–
780 169.
- 781 Evans, K.A., Bickle, M.J., Skelton, A.D.L., Hall, M., Chapman, H., 2002. Reductive
782 deposition of graphite at lithological margins in East Central Vermont: a Sr, C and O

783 isotope study. *Journal of metamorphic Geology* 20, 781–798. doi:10.1046/j.1525-
784 1314.2002.00403.x

785 Facq, S.B., Daniel, I., Montagnac, G., Cardon, H., Sverjensky, D.A., 2014. In situ Raman
786 study and thermodynamic model of aqueous carbonate speciation in equilibrium with
787 aragonite under subduction zone conditions. *Geochimica et Cosmochimica Acta* 132,
788 375–390. doi:10.1016/j.gca.2014.01.030

789 Fournier, M., Jolivet, L., Goff, B., Dubois, R., 1991. Alpine Corsica metamorphic core
790 complex. *Tectonics* 10, 1173–1186.

791 Gabalda, S., Beyssac, O., Jolivet, L., Agard, P., Chopin, C., 2009. Thermal structure of a
792 fossil subduction wedge in the Western Alps. *Terra Nova* 21, 28–34. doi:10.1111/j.1365-
793 3121.2008.00849.x

794 Galvez, M.E., Beyssac, O., Martinez, I., Benzerara, K., Chaduteau, C., Malvoisin, B.,
795 Malavieille, J., 2013. Graphite formation by carbonate reduction during subduction.
796 *Nature Geoscience* 6, 473–477. doi:10.1038/ngeo1827

797 Galy, V., Beyssac, O., France-Lanord, C., Eglinton, T., 2008. Recycling of graphite during
798 Himalayan erosion: A geological stabilization of carbon in the crust. *Science* 322, 943–
799 945.

800 Gorman, P.J., Kerrick, D.M., Connolly, J.A.D., 2006. Modeling open system metamorphic
801 decarbonation of subducting slabs. *Geochemistry, Geophysics, Geosystems* 7, 1–21.
802 doi:10.1029/2005GC001125

803 Groppo, C., Castelli, D., 2010. Prograde P–T Evolution of a Lawsonite Eclogite from the
804 Monviso Meta-ophiolite (Western Alps): Dehydration and Redox Reactions during
805 Subduction of Oceanic FeTi-oxide Gabbro. *Journal of Petrology* 51, 2489–2514.
806 doi:10.1093/petrology/egq065

807 Hayes, J.M., Waldbauer, J.R., 2006. The carbon cycle and associated redox processes through
808 time. *Philosophical Transactions of the Royal Society B: Biological Sciences* 361, 931–
809 950. doi:10.1098/rstb.2006.1840

810 Hermann, J., Spandler, C., Hack, A., Korsakov, A., 2006. Aqueous fluids and hydrous melts
811 in high-pressure and ultra-high pressure rocks: Implications for element transfer in
812 subduction zones. *Lithos* 92, 399–417. doi:10.1016/j.lithos.2006.03.055

813 Holloway, J.R., 1984. Graphite-CH₄-H₂O-CO₂ equilibria at low-grade metamorphic
814 conditions. *Geology* 12, 455–458.

815 Kelemen, P.B., Manning, C.E., 2015. Reevaluating carbon fluxes in subduction zones, what
816 goes down, mostly comes up. *PNAS* 112, E3997–E4006. doi:10.1073/pnas.1507889112

817 Lagabrielle, Y., Lemoine, M., 1997. Alpine, Corsican and Apennine ophiolites: the slow-
818 spreading ridge model. *Comptes Rendus de l'Académie des Sciences* 325, 909–920.

819 Lagabrielle, Y., Vitale Brovarone, A., Ildefonse, B., 2015. Fossil oceanic core complexes
820 recognized in the blueschist metaophiolites of Western Alps and Corsica. *Earth Science*
821 *Reviews* 141, 1–26. doi:10.1016/j.earscirev.2014.11.004

822 Lemoine, M., 2003. Schistes lustrés from Corsica to Hungary : back to the original sediments
823 and tentative dating of partly azoic metasediments 174, 197–209.

824 Luque, F.J., Ortega, L., Barrenechea, J.F., Millward, D., Beyssac, O., Huizenga, J.-M., 2009.
825 Deposition of highly crystalline graphite from moderate-temperature fluids. *Geology* 37,
826 275–278. doi:10.1130/G25284A.1

827 Mori, Y., Shigeno, M., Nishiyama, T., 2014. Fluid-metapelite interaction in an ultramafic
828 mélange: implications for mass transfer along the slab-mantle interface in subduction
829 zones 66, 1–8. doi:10.1186/1880-5981-66-47

830 Mullis, J., Dubessy, J., Poty, B., O'Neil, J., 1994. Fluid regimes during late stages of a
831 continental collision: Physical, chemical, and stable isotope measurements of fluid
832 inclusions in fissure quartz from a geotraverse through the Central Alps, Switzerland.
833 *Chemical Geology* 58, 2239–2267. doi:10.1016/0016-7037(94)90008-6

834 Newton, R.C., Manning, C.E., 2009. Hydration state and activity of aqueous silica in H₂O-
835 CO₂ fluids at high pressure and temperature. *American Mineralogist* 94, 1287–1290.
836 doi:10.2138/am.2009.3287

837 Nitsch, K.-H., 1972. Das P-T-X_{CO2} Stabilitätsfeld von Lawsonit. *Contributions to Mineralogy*
838 *and Petrology* 34, 116–134.

839 Pattison, D.R.M., 2006. The fate of graphite in prograde metamorphism of pelites: An
840 example from the Ballachulish aureole, Scotland. *Lithos* 88, 85–99.
841 doi:10.1016/j.lithos.2005.08.006

842 Piccoli, F., Hermann, J., Pettke, T., Connolly, J.A.D., Kempf, E.D., Duarte, J.F.V., 2019.
843 Subducting serpentinites release reduced, not oxidized, aqueous fluids. *Scientific Reports*
844 9, 1–7. doi:10.1038/s41598-019-55944-8

845 Piccoli, F., Vitale Brovarone, A., Beyssac, O., Martinez, I., Ague, J.J., Chaduteau, C., 2016.
846 Carbonation by fluid–rock interactions at high-pressure conditions: Implications for
847 carbon cycling in subduction zones. *Earth and Planetary Science Letters* 445, 146–159.
848 doi:10.1016/j.epsl.2016.03.045

849 Plank, T., 2014. 4.17 The Chemical Composition of Subducting Sediments, 2nd ed, *The*
850 *Crust*. Elsevier Ltd. doi:10.1016/B978-0-08-095975-7.00319-3

851 Poli, S., 2015. Carbon mobilized at shallow depths in subduction zones by carbonatitic
852 liquids. *Nature Geoscience* 8, 633–636. doi:10.1038/ngeo2464

853 Polino, R., Lemoine, M., 1984. Détritisme mixte d'origine continentale et océanique dans les
854 sédiments jurassico-crétacés supra-ophiolitiques de la Téthys Ligure: la série du Lago
855 Nero (Alpes Occidentales franco-italiennes). *Comptes Rendus de l'Académie des*
856 *Sciences* 298, 359–364.

857 Ravna, E.J.K., Andersen, T.B., Jolivet, L., de Capitani, C., 2010. Cold subduction and the
858 formation of lawsonite eclogite - constraints from prograde evolution of eclogitized
859 pillow lava from Corsica 28, 381–395. doi:10.1111/j.1525-1314.2010.00870.x

860 Schwartz, S., Guillot, S., Reynard, B., Lafay, R., Debret, B., Nicollet, C., Lanari, P., Auzende,
861 A.L., 2013. Pressure–temperature estimates of the lizardite/antigorite transition in high
862 pressure serpentinites. *Lithos* 178, 197–210. doi:10.1016/j.lithos.2012.11.023

863 Souche, A., Beyssac, O., Andersen, T.B., 2012. Thermal structure of supra-detachment
864 basins: a case study of the Devonian basins of western Norway. *Journal of the Geological*
865 *Society* 169, 427–434. doi:10.1144/0016-76492011-155

866 Tarantola, A., Mullis, J., Vennemann, T., Chemical, J.D., de Capitani, C., 2007. Oxidation of
867 methane at the CH₄/H₂O–(CO₂) transition zone in the external part of the Central Alps,
868 Switzerland: evidence from stable isotope investigations. *Chemical Geology* 237, 329–
869 357. doi:10.1016/j.chemgeo.2006.07.007

870 Tiraboschi, C., 2018. Experimental determination of magnesia and silica solubilities in
871 graphite-saturated and redox-buffered high-pressure COH fluids in equilibrium with
872 forsterite + enstatite and magnesite + enstatite. *Contributions to Mineralogy and Petrology*
873 173, 1–17. doi:10.1007/s00410-017-1427-0

874 Tumiati, S., Malaspina, N., 2019. Redox processes and the role of carbon-bearing volatiles
875 from the slab–mantle interface to the mantle wedge. *Journal of the Geological Society*
876 176, 388–397. doi:10.1144/jgs2018-046

877 Tumiati, S., Tiraboschi, C., Miozzi, F., Vitale Brovarone, A., Manning, C.E., Sverjensky,
878 D.A., Milani, S., Poli, S., 2020. Dissolution susceptibility of glass-like carbon versus
879 crystalline graphite in high-pressure aqueous fluids and implications for the behavior of
880 organic matter in subduction zones. *Geochimica et Cosmochimica Acta* 273, 383–402.
881 doi:10.1016/j.gca.2020.01.030

882 Tumiati, S., Tiraboschi, C., Sverjensky, D.A., Pettke, T., Recchia, S., Ulmer, P., Miozzi, F.,
883 Poli, S., 2017. Silicate dissolution boosts the CO₂ concentrations in subduction fluids.
884 *Nature Communications* 1–11. doi:10.1038/s41467-017-00562-z

885 Vitale Brovarone, A., Agard, P., Monié, P., Chauvet, A., Rabaute, A., 2018a. Tectonic and
886 metamorphic architecture of the HP belt of New Caledonia. *Earth Science Reviews* 178,
887 48–67. doi:10.1016/j.earscirev.2018.01.006

888 Vitale Brovarone, A., Alard, O., Beyssac, O., Martin, L., Picatto, M., 2014a. Lawsonite
889 metasomatism and trace element recycling in subduction zones. *Journal of metamorphic*
890 *Geology* 32, 489–514. doi:10.1111/jmg.12074

- 891 Vitale Brovarone, A., Beyssac, O., 2014. Lawsonite metasomatism: A new route for water to
892 the deep Earth. *Earth and Planetary Science Letters* 393, 275–284.
893 doi:10.1016/j.epsl.2014.03.001
- 894 Vitale Brovarone, A., Beyssac, O., Malavieille, J., Molli, G., Beltrando, M., Compagnoni, R.,
895 2013. Stacking and metamorphism of continuous segments of subducted lithosphere in a
896 high-pressure wedge: The example of Alpine Corsica (France). *Earth Science Reviews*
897 116, 35–56. doi:10.1016/j.earscirev.2012.10.003
- 898 Vitale Brovarone, A., Chu, X., Martin, L.A.J., Ague, J.J., Monié, P., Groppo, C., Martinez, I.,
899 Chaduteau, C., 2018b. Intra-slab COH fluid fluxes evidenced by fluid-mediated
900 decarbonation of lawsonite eclogite-facies altered oceanic metabasalts. *Lithos* 304-307,
901 211–229. doi:10.1016/j.lithos.2018.01.028
- 902 Vitale Brovarone, A., Martinez, I., Elmaleh, A., Compagnoni, R., Chaduteau, C., Ferraris, C.,
903 Esteve, I., 2017. Massive production of abiotic methane during subduction evidenced in
904 metamorphosed ophicarbonates from the Italian Alps. *Nature Communications* 8, 14134–
905 13. doi:10.1038/ncomms14134
- 906 Vitale Brovarone, A., Picatto, M., Beyssac, O., Lagabrielle, Y., Castelli, D., 2014b. The
907 blueschist–eclogite transition in the Alpine chain: P–T paths and the role of slow-
908 spreading extensional structures in the evolution of HP–LT mountain belts.
909 *Tectonophysics* 615-616, 96–121. doi:10.1016/j.tecto.2014.01.001
- 910 Wilson, C.R., Spiegelman, M., van Keken, P.E., Hacker, B.R., 2014. Fluid flow in subduction
911 zones: The role of solid rheology and compaction pressure. *Earth and Planetary Science*
912 *Letters* 401, 261–274. doi:10.1016/j.epsl.2014.05.052
- 913 Zhang, S., Ague, J.J., Brovarone, A.V., 2018. Degassing of organic carbon during regional
914 metamorphism of pelites, Wepawaug Schist, Connecticut, USA. *Chemical Geology* 490,
915 30–44. doi:10.1016/j.chemgeo.2018.05.003
- 916 Ziegenbein, D., Johannes, W., 1980. Graphite in C-H-O fluids: unsuitable compound to buffer
917 fluid composition at temperatures up to 700°C. *Neues Jahrbuch Mineralogie Monatshefte*
918 7, 289–305.

920

921

922 **Figure Captions**

923 **Figure 1**

924 Metamorphic maps of the study areas in Alpine Corsica (a) and Western Alps (b), modified
925 after Vitale Brovarone, Picatto et al. (2014) and Schwartz et al., (2013), respectively.
926 Estimated peak conditions based on Raman Spectroscopy of Carbonaceous Material and
927 thermodynamics are also shown. In Alpine Corsica, the lower-grade T appearance of CM
928 leaching in metasomatic aureoles corresponds to the field-based isograd for lawsonite
929 metasomatism (~ 370 °C), while in the Western Alps, similar processes were found at lower T
930 in the range of 330-340 °C.

931

932 **Figure 2**

933 (a-c) Examples of lawsonite-bearing, CM depleted reaction zones in contact with
934 mafic/ultramafic blocks in Alpine Corsica (See also Fig. 5 for a detailed profile). (a-a')
935 Example of a relatively thin reaction zone in contact with a small metagabbro block. The
936 bleaching zone next to the contact (red line) is highlighted in (a'), which also show the

937 distribution of CM-rich lawsonite blasts (small, elongated rectangles). The size of the blasts in
938 not to scale). (b-c) Close-up and photomicrograph of the CM-depleted zone marked by the red
939 box in (a'). In (c), note the presence of a CM-rich foliation preserved in the lawsonite blasts.
940 (d-f) Example of lawsonite-bearing, CM-depleted individual layers within the
941 metasedimentary suite in the absence of mafic/ultramafic blocks (d-f). In (f), note the
942 presence of CM-rich lawsonite crystals preserved in a CM-poor matrix.

943

944 **Figure 3**

945 Examples of lawsonite-bearing, CM-depleted reaction zones in contact with mafic/ultramafic
946 rocks in the Western Alps. (a-d) General distribution and patterns of CM-leaching and
947 lawsonite precipitation (bleached area in a') around metabasaltic blocks (green blocks in (a')).
948 The size of the lawsonite blasts (small, elongated rectangles in (a')) is not to scale. (b-d)
949 Close-ups and photomicrograph of the CM-depleted zone marked by the red box in (a'). In
950 (d), note the presence of a CM-rich foliation preserved in the lawsonite blasts. (e-h) General
951 distribution and patterns of CM-leaching and lawsonite precipitation (bleached area in e') in a
952 complexly deformed calcschist + metachert sequence in contact with an ultramafic block
953 (green zone in (e')). The size of the lawsonite blasts (small, elongated rectangles in (e')) is not
954 to scale and is confined to the calcschist layers initially present in the rock. (f-h) Close-ups
955 and photomicrograph of the CM-depleted zone marked by the red box in (e'). In (g-h), note
956 the presence of a CM-rich foliation preserved in the lawsonite blasts in a chlorite-lawsonite
957 rich (g) and a quartz-carbonate-mica (h) layer.

958

959 **Figure 4**

960 Microstructural features of lawsonite-rich metasomatic rocks showing evidence for fluid-
961 mediated CM dissolution in both Alpine Corsica (a-c) and Western Alps (d-f) blueschist-
962 facies units. (b,d) are from metasomatic aureoles surrounding ultramafic block, whereas all
963 others surround metagabbro blocks. Note the abundance of CM (\pm rutile needles) included in
964 lawsonite. Note also, in (a-b), the presence of a CM-free rim in the lawsonite crystals. The T
965 estimates for each panel are from Vitale Brovarone et al. (2014b) and Schwartz et al., (2013).

966

967 **Figure 5**

968 Field image and characteristic microstructural features of the selected metasomatic aureole.
969 The outcrop exposes the contact (red line) between a metagabbro block (right) and the
970 embedding metasedimentary rocks. The metasediment shows a progressive compositional and
971 mineralogical variation towards the contact zone leading to an intense bleaching of the rock.
972 Z1(least altered or not altered): phengite(~45vol%), chlorite(40%), quartz(10), accessory

973 phases(5%); Z2: phengite(30%), chlorite(35%), quartz(15%), lawsonite(15%), accessory
974 phases(5%); Z3: phengite(25%), chlorite(25%), quartz(30%), lawsonite(15%), accessory
975 phases(5%); Z4: phengite(15%), chlorite(15%), quartz(50%), albite(10%), lawsonite(5%)
976 accessory phases(5%); Z5: albite(40%), blue-amphibole(30%), chlorite(20%), quartz(5%),
977 accessory phases(5%). Photomicrographs are reported for each zone of the least to the most
978 altered pelitic schist (bottom).

979

980 **Figure 6**

981 Whole-rock C content across the reaction zone shown in Figure 5. Note the progressive
982 decrease in organic C, present as CM in the studied samples, towards the contact zone, and
983 the main drops at the Z2-Z3 and Z3-Z4 boundaries. Note that only one sample (sample 2f)
984 contain little C other than organic C (0.5 wt%) and interpreted as carbonate. For each zone,
985 the average distance from the metagabbro is indicated. The “0” value corresponds to the
986 interface between the metagabbro and the metapelite.

987

988 **Figure 7**

989 (a-c) Representative Raman spectra of CM in the studied samples and corresponding R2
990 values. The defect bands (D1-D2) and the associated R2 values decrease from (a) to (c).
991 Rather crystalline graphite in (c) has very small D1-D2 bands. See Figure 8 for a complete
992 Raman characterization of CM from Z1 to Z5. Spectrum (a) is characteristic of the dominant
993 CM cluster in samples unaffected by fluid-mediated transformations and of the CM preserved
994 as inclusions in fluid-precipitated minerals such as lawsonite. Spectra (b) and (c) are
995 representative of the dominant CM cluster in the matrix of samples characterized by intense
996 fluid-mediated transformations, and is also present as minor cluster in the protolith metapelite
997 unaffected by metasomatism. Examples of microstructural distribution of different types of
998 CM in the studied samples are shown (d-e), with higher R2 CM preserved as inclusions in
999 lawsonite, and lower R2 CM preserved in the rock matrix. See Figure 8 and Table 2 for
1000 distribution of R2 values across the selected reaction zone.

1001

1002 **Figure 8**

1003 Results of RSCM and characteristic photomicrographs for the different reaction zones. Z1:
1004 least altered metapelite including dark, CM-rich titanite (Ttn); Z2: lawsonite-bearing
1005 metapelite. Note the precipitation of lawsonite in the CM-rich metapelite; Z3: lawsonite-
1006 bearing schist. Here, dark, CM-rich lawsonite (same as Z2) floats in a bleached, CM-poor
1007 matrix; Z4: quartz-albite schist preserving relicts of CM-rich lawsonite; Blue-amphibole-
1008 chlorite schist. Rare relicts of CM are present as inclusions in titanite. The histograms to the

1009 right show the structural variation of CM throughout the reaction zone based on Raman
1010 analysis, expressed as R2 (relative area of the defect band of CM in Raman spectra Section
1011 4.2). CM_{inc} in lawsonite and titanite shows constant R2 values throughout the reaction zone,
1012 except for the more internal zone where it shows a much lower R2. CM_m is similar to CM_{inc}
1013 in Z1, whereas it shifts towards lower R2 values approaching the contact zone. In Z5, any CM
1014 was found in the matrix.

1015

1016 **Figure 9**

1017 Concentration ratio diagram for fluid-mobile element profiles across the interaction zone.

1018 Note the depletion in K, Ba, Rb and Cs on both sides of the contact zone suggesting a

1019 dominantly advective mechanism of mass transport.

1020

1021 **Figure 10**

1022 Estimated time-integrated fluid fluxes required to mobilize the calculated CM loss from each
1023 reaction zone. For each P-T condition, results for both glass-like C (lower bounds) and
1024 crystalline graphite (upper bounds) are shown. The more disorder CM cluster in the selected
1025 samples is expected to lie in between. The values on the vertical axis are dependent on the
1026 parameter n, which is the Log of L (distance of the reaction front). See Figure 11 for graphical
1027 examples.

1028

1029 **Figure 11**

1030 Schematic representation of the distribution and magnitude of channelized fluid flow within
1031 the blueschist-facies, block-in-matrix units of Alpine Corsica and Western Alps. Values of
1032 time-integrated fluid flux (in m³/m²) refer to the minimum fluxes required to mobilize CM at
1033 P ranging from ~1 to ~2 GPa and T ranging from 300 to about 450 °C. L = distance of
1034 reaction front propagation.

1035

1036 **Table Captions**

1037 **Table 1.** Bulk organic C and total CO₂ content in the selected samples across the
1038 metasomatic aureole.

1039

1040 **Table 2.** RSCM R2 values of matrix and inclusion CM throughout the studied reaction zone.

1041

1042 **Table 3.** Calculated fractional mass change and organic C loss per 100g of rock for Zr, Hf,
1043 and Th.

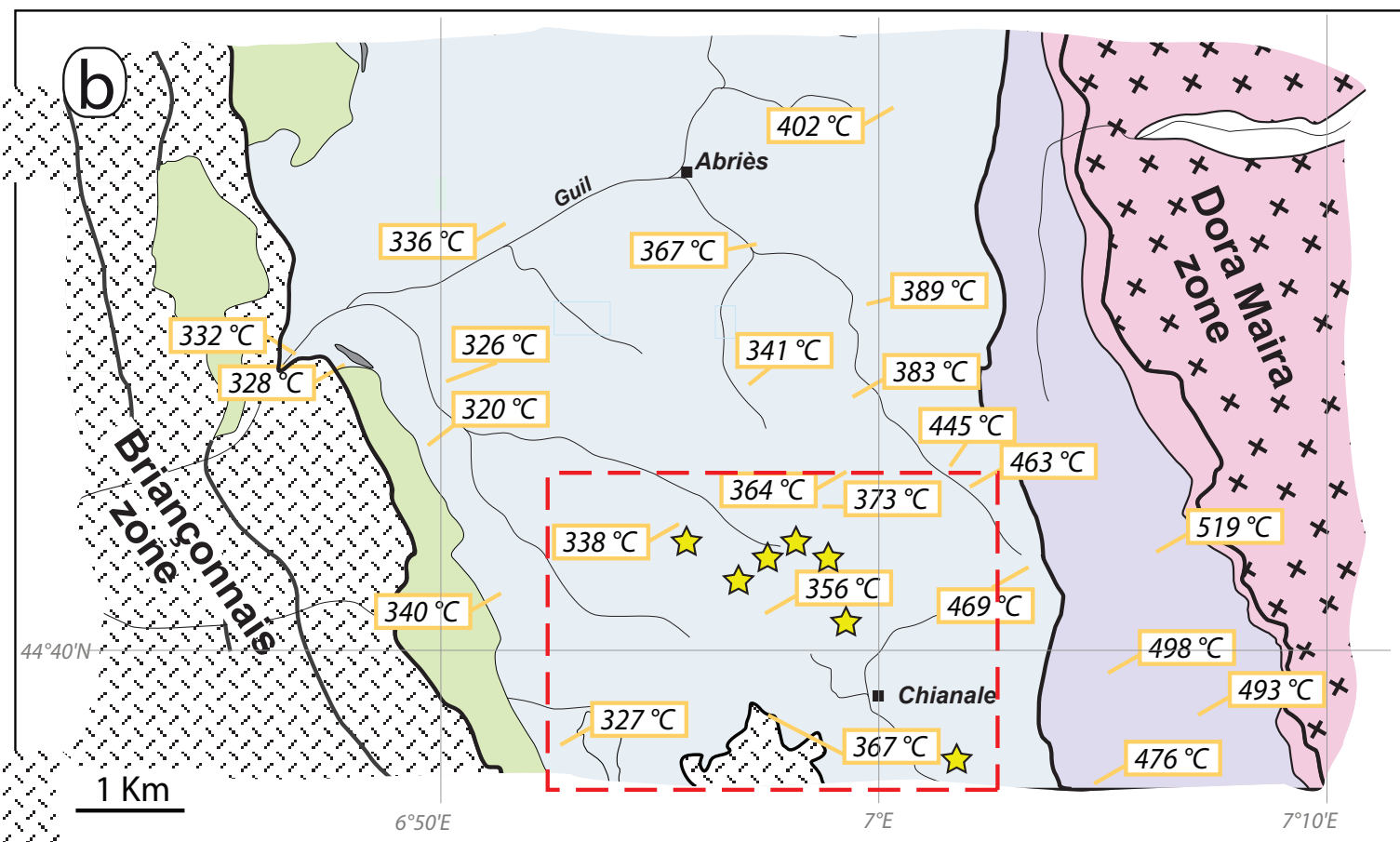
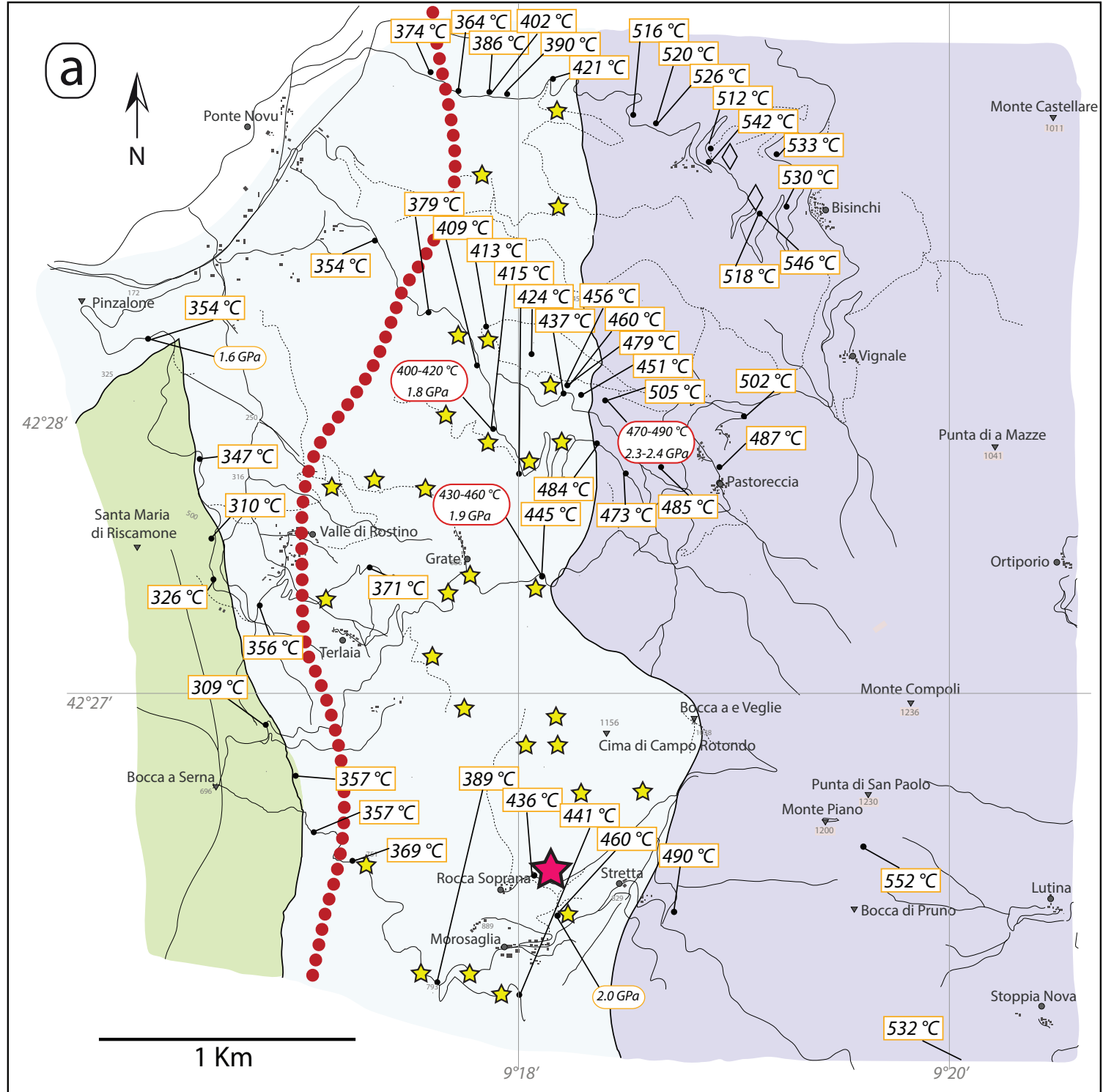
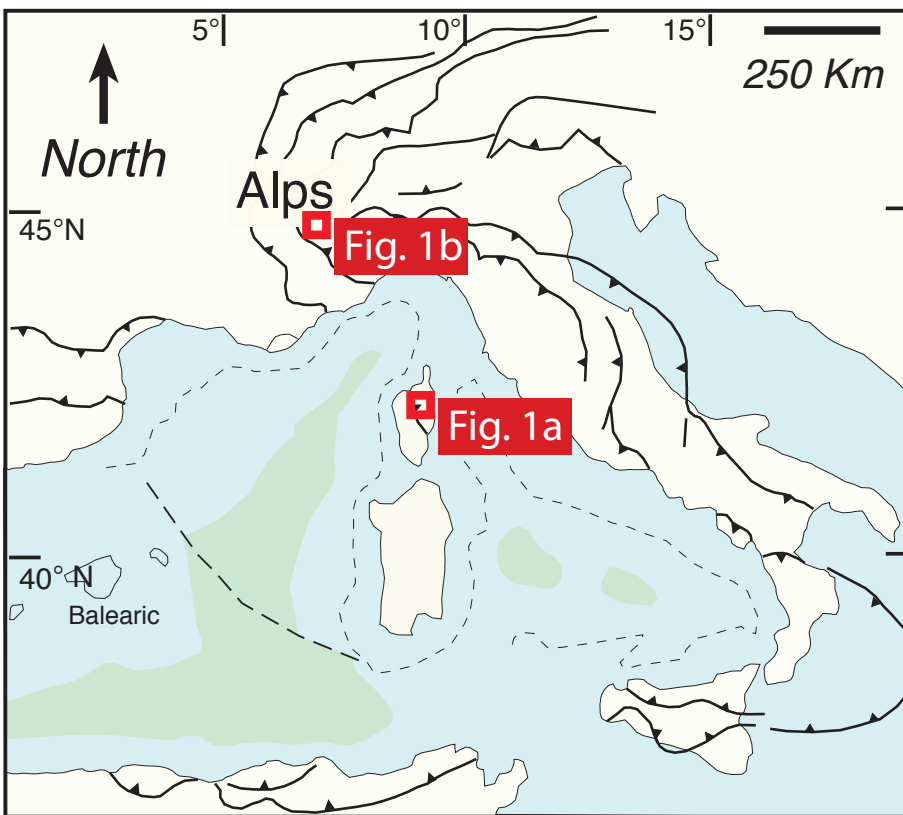
1044

1045 **Table 4.** Fluid component speciation considered for mass balances and flux estimates,
1046 calculated by thermodynamic modelling of COH fluids saturated with graphite and glass-like
1047 carbon.

1048

1049 **Table 5.** Calculated time-integrated fluid fluxes at H₂O-maximum. For each sample, q_{TI} is
1050 calculated by considering the CM fractional change relative to the average of Z1.

1051



Subgreenschist zone

Blueschist zone (BSZ)

Eclogite zone (EZ)

Dora Maira

Dora Maira

Field-based isograd for lawsonite metasomatism

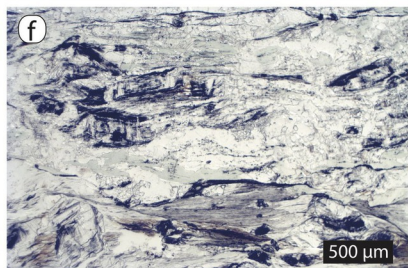
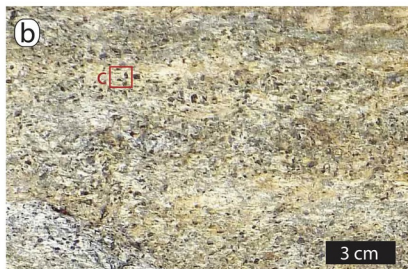
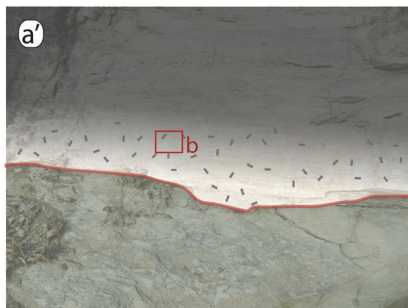
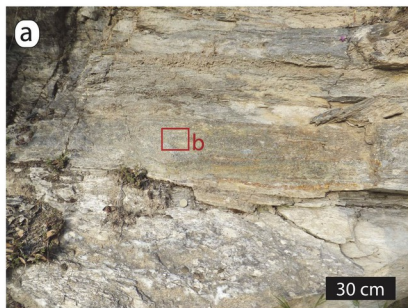
Lawsonite-bearing metasomatic aureoles

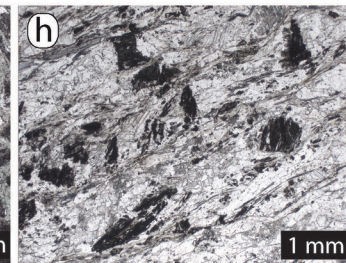
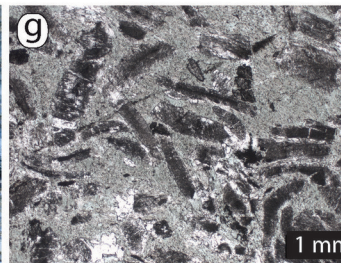
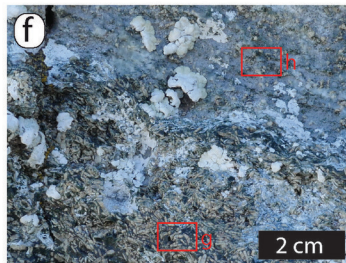
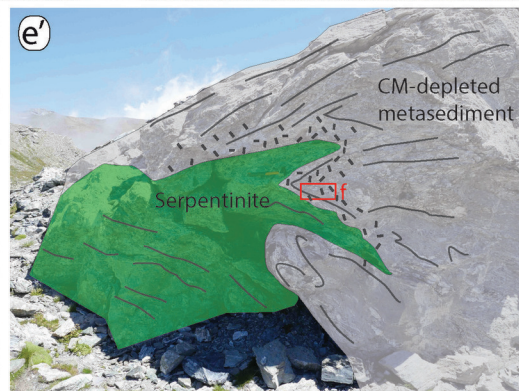
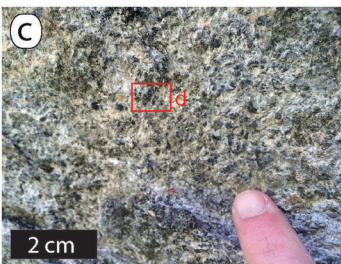
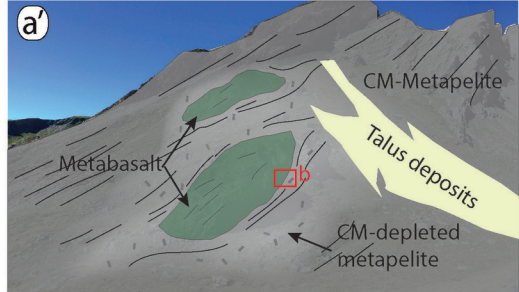
Considered metasomatic aureole

Investigated area (W. Alps)

RSCM (T_{max}) (see caption for references)

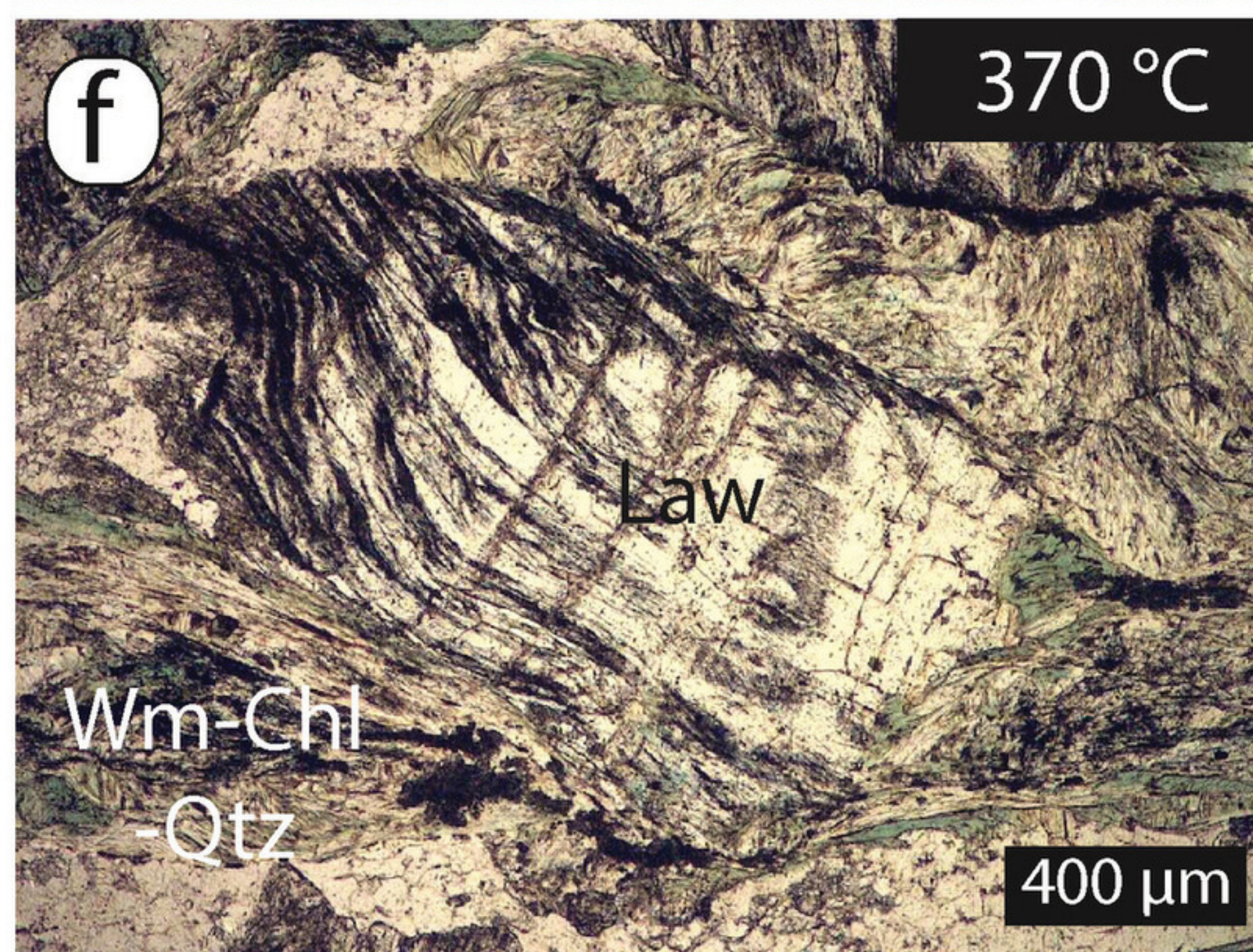
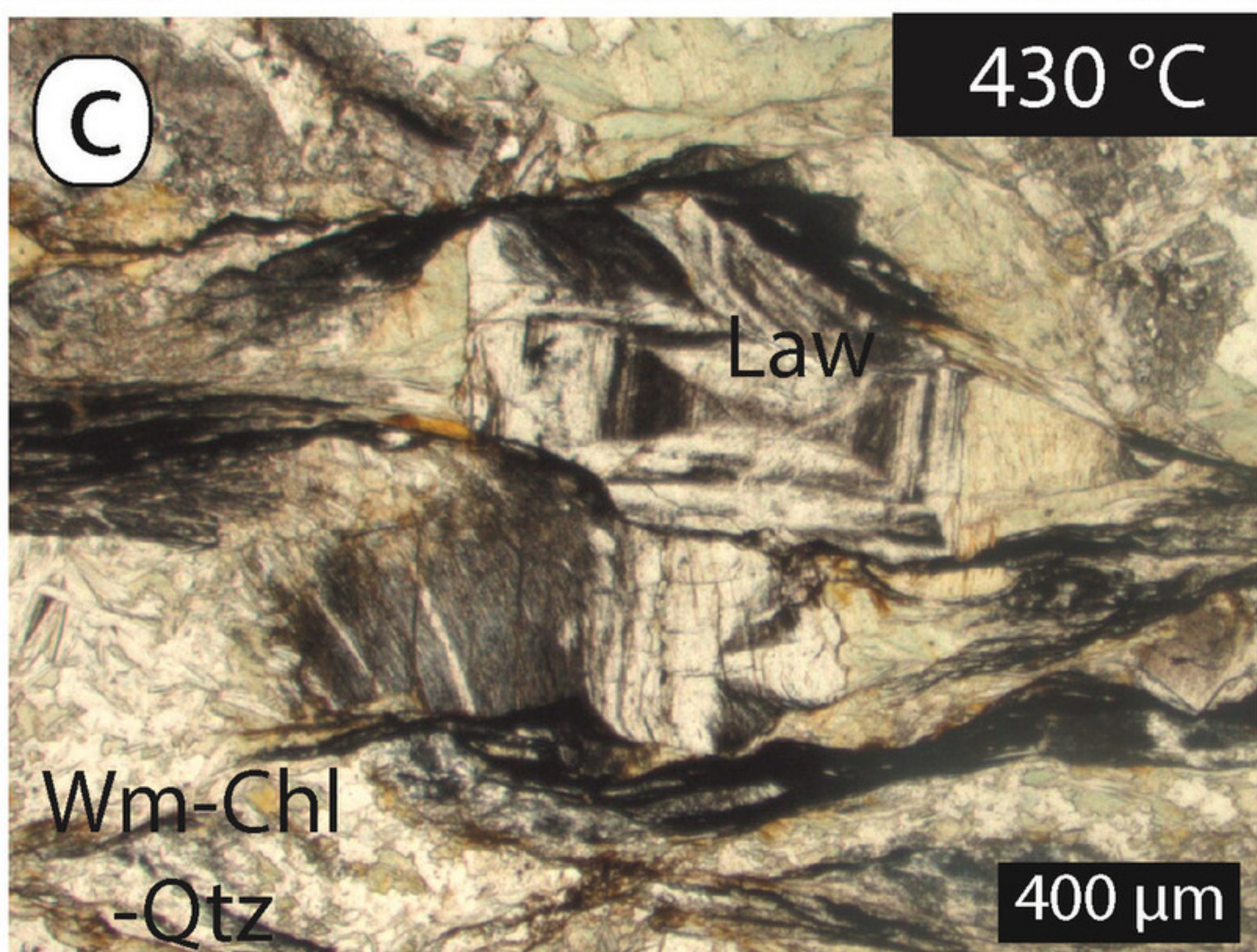
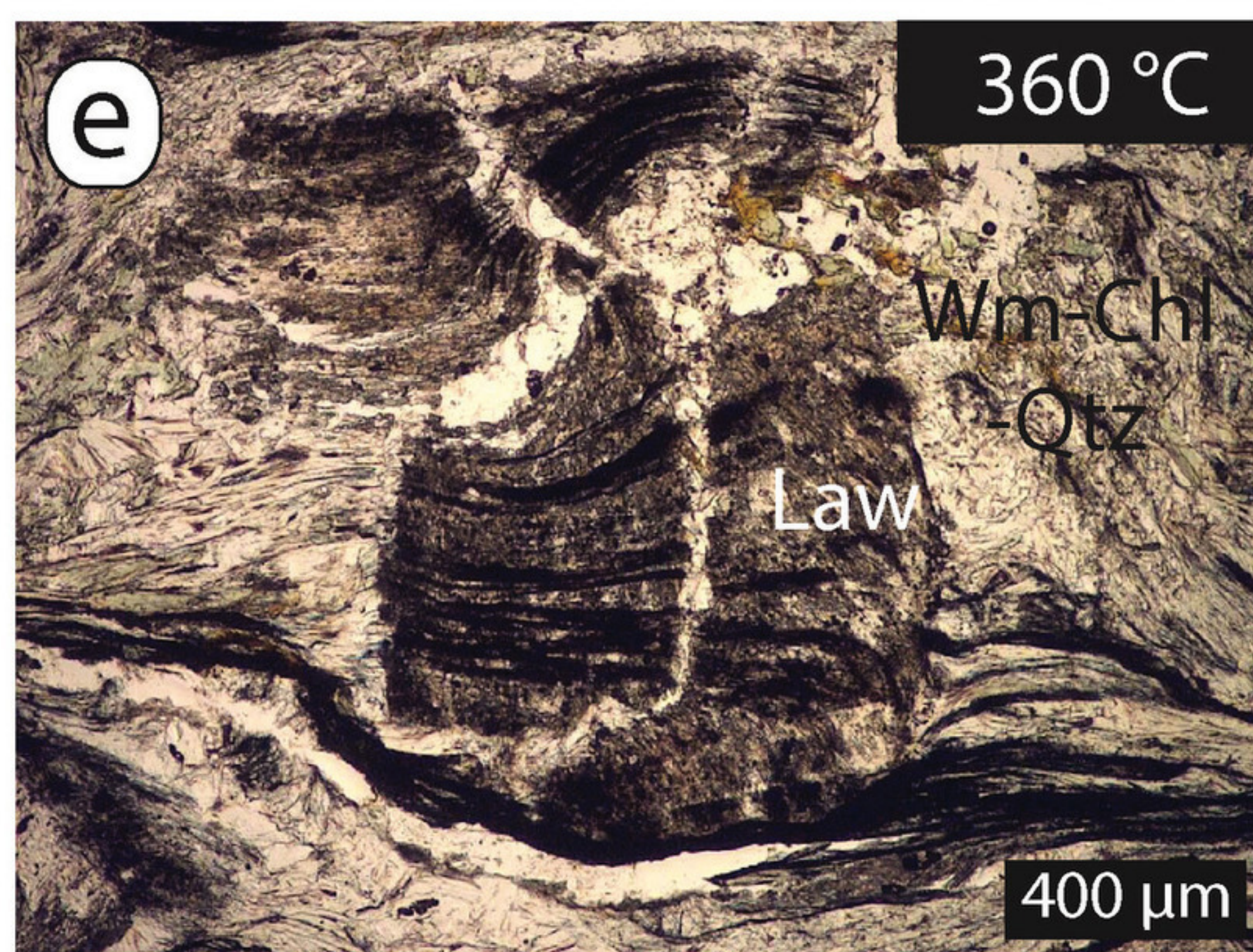
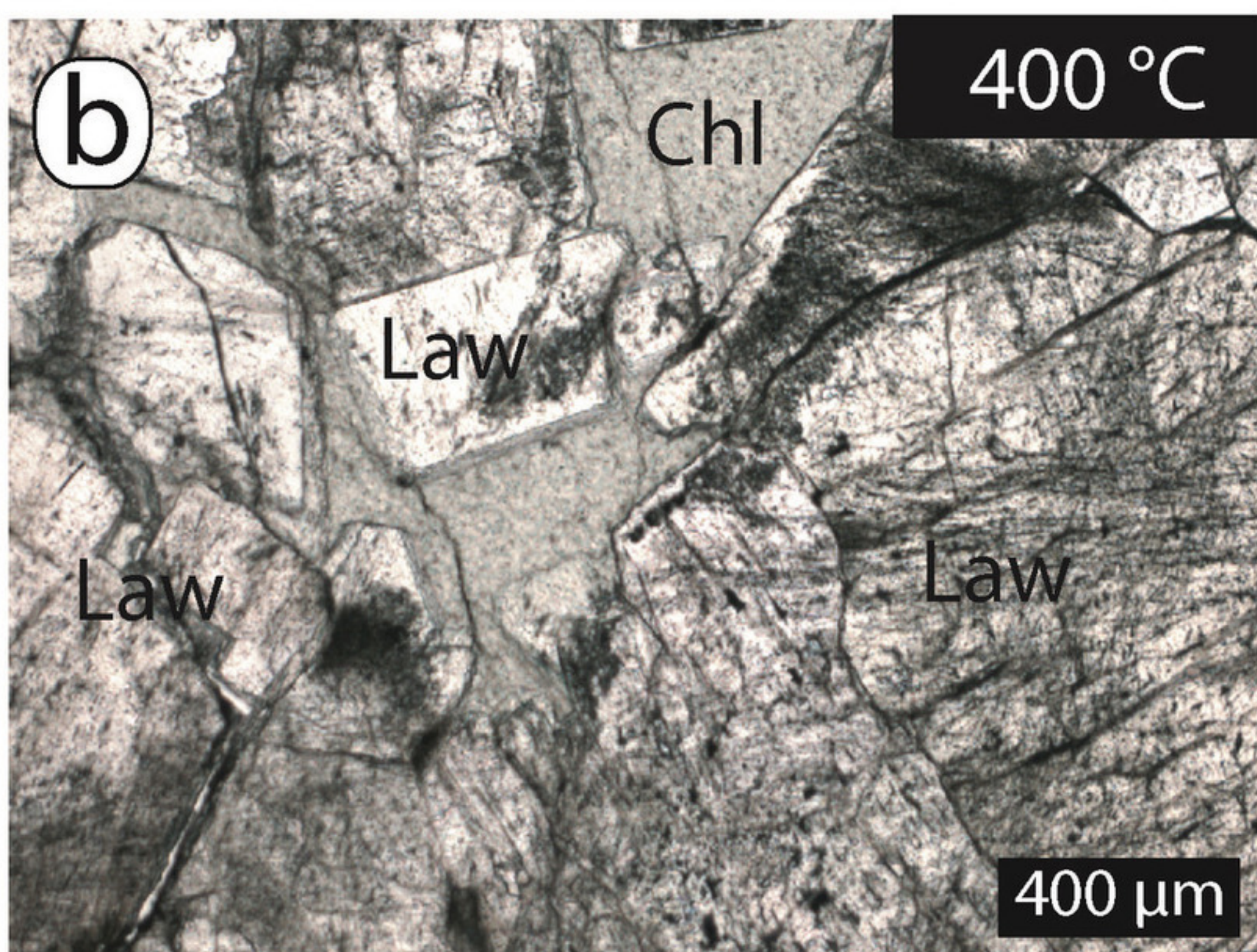
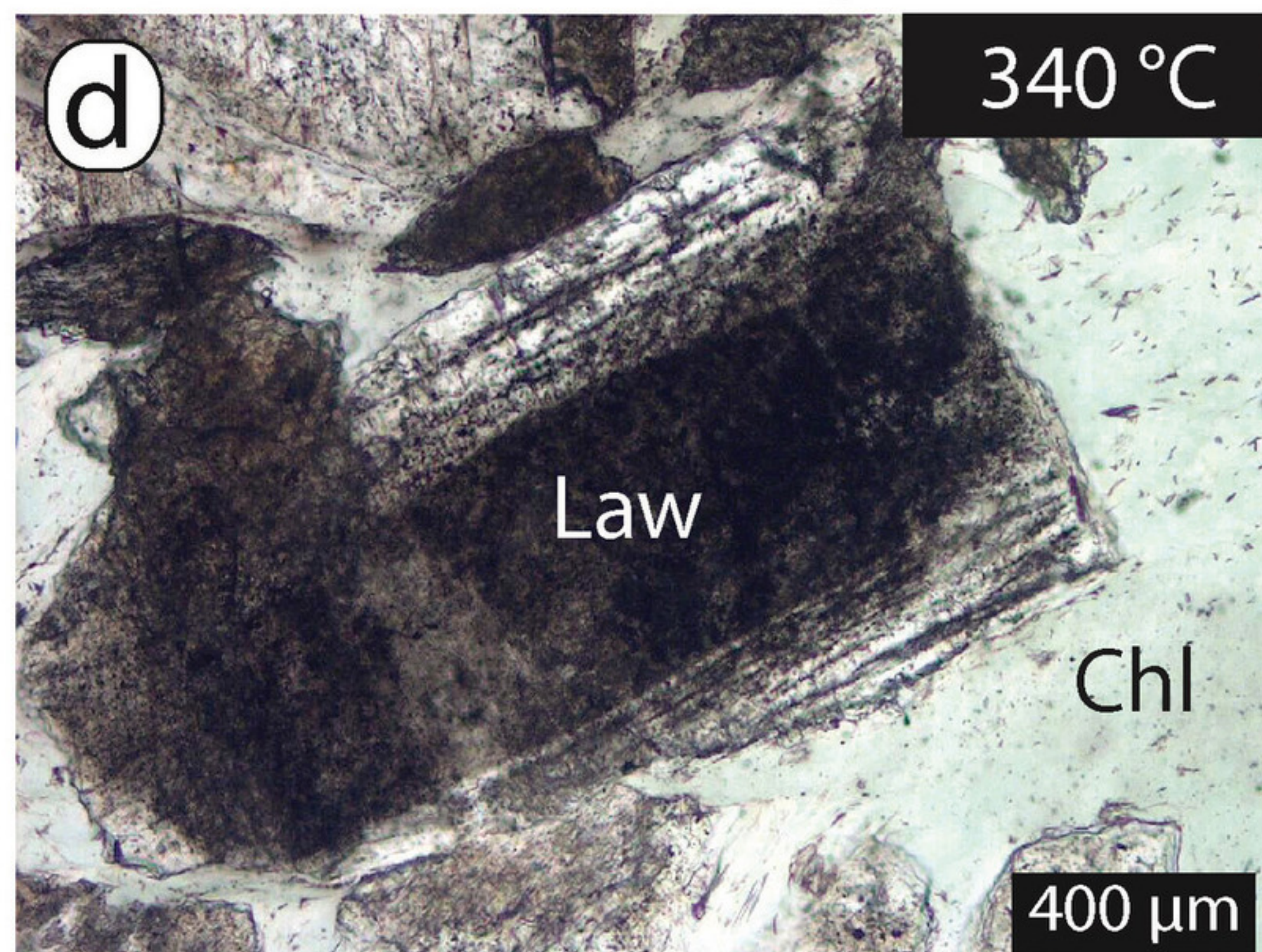
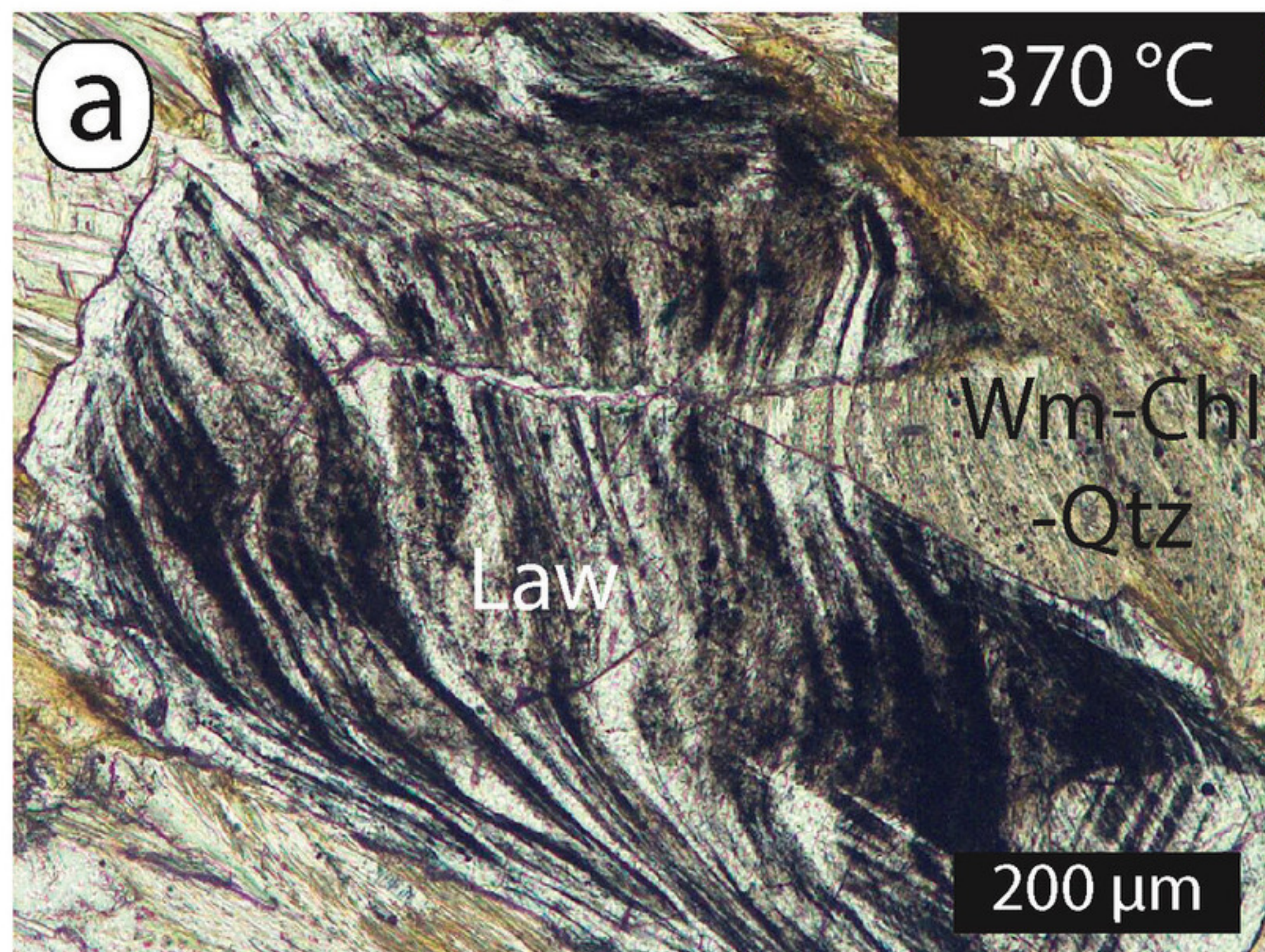
PT (see caption for references)

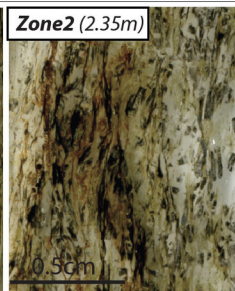
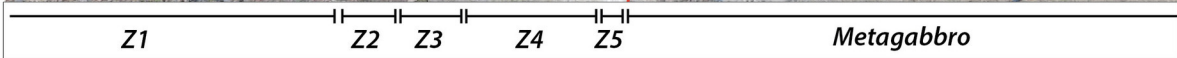


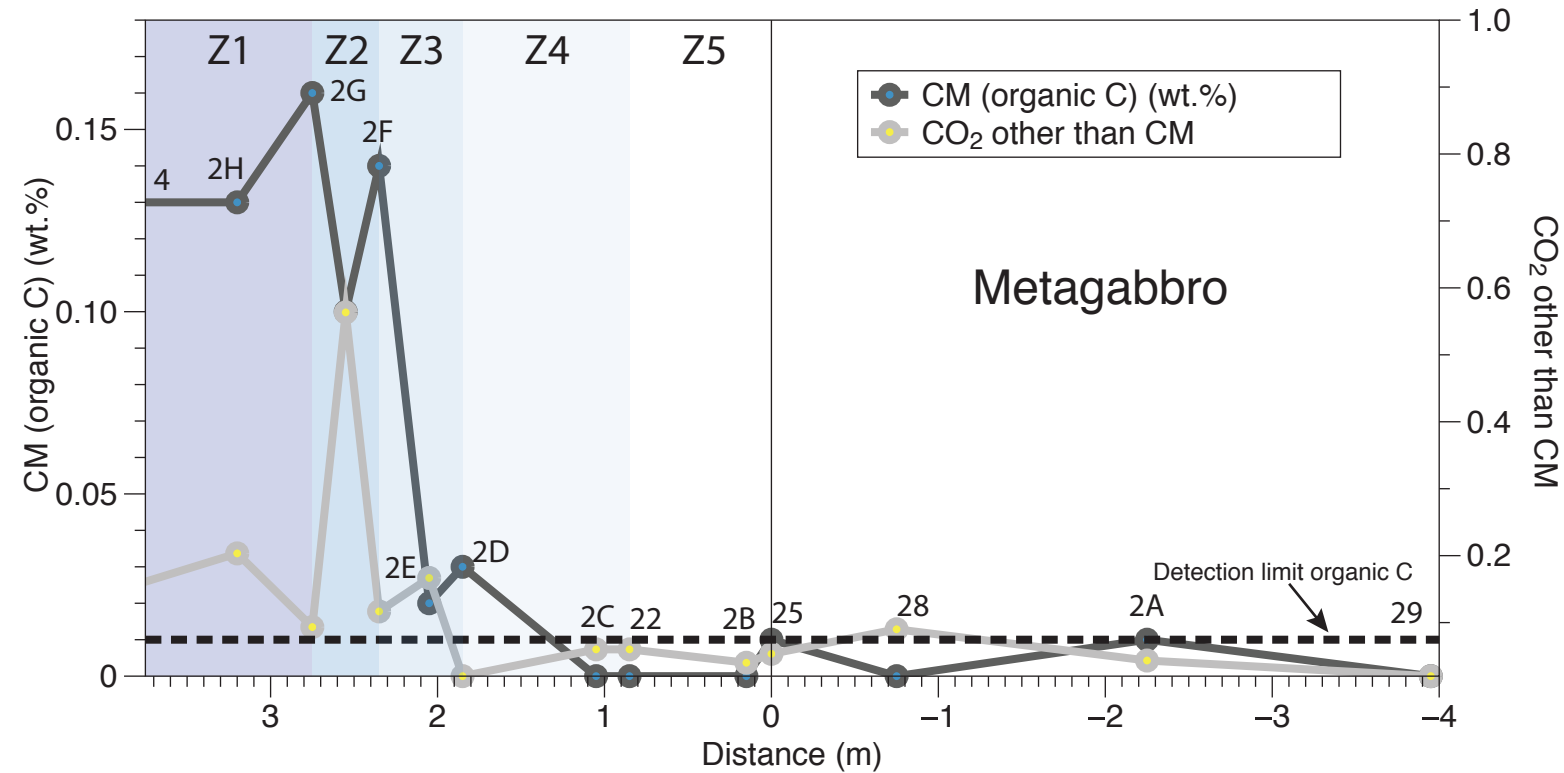


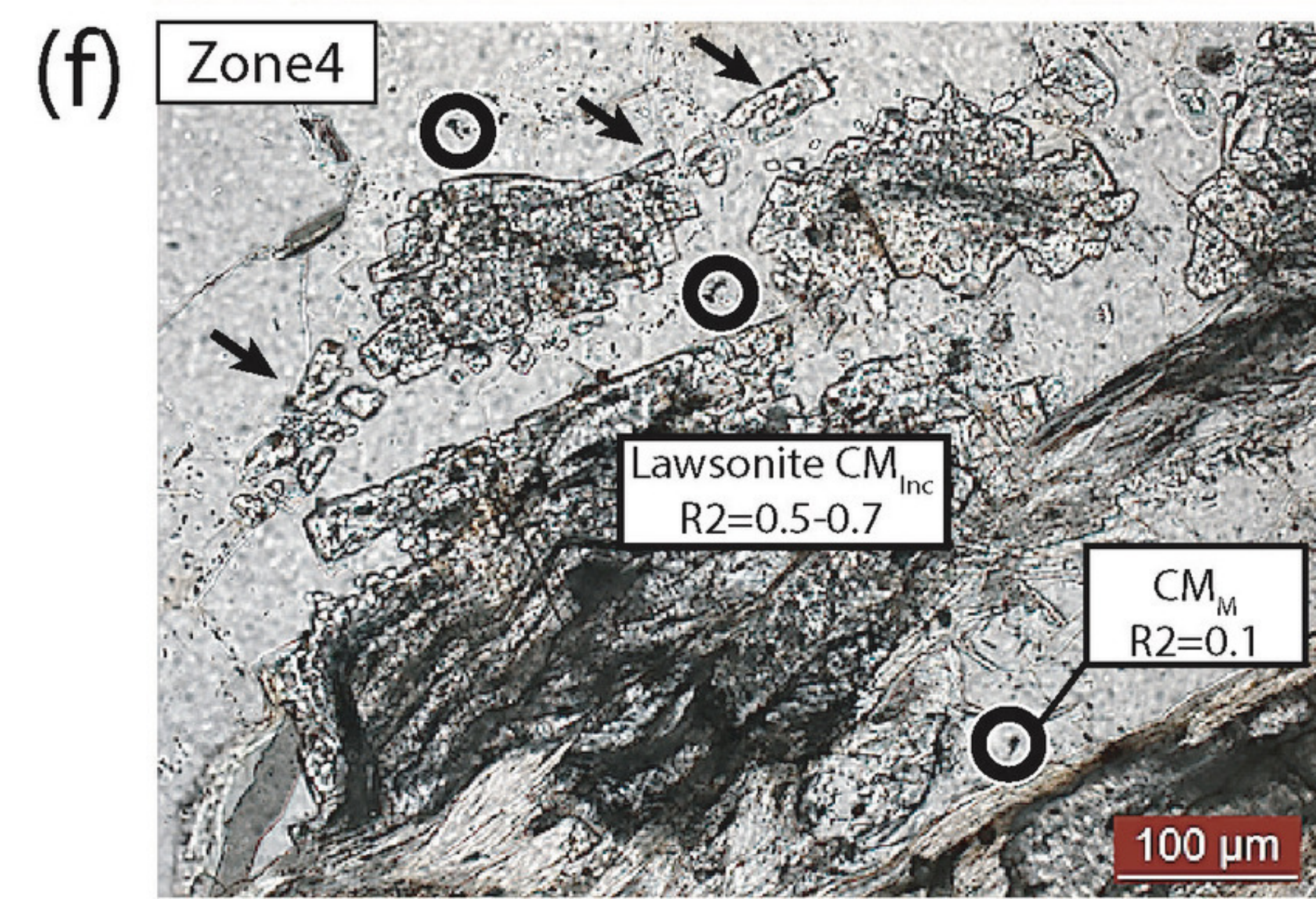
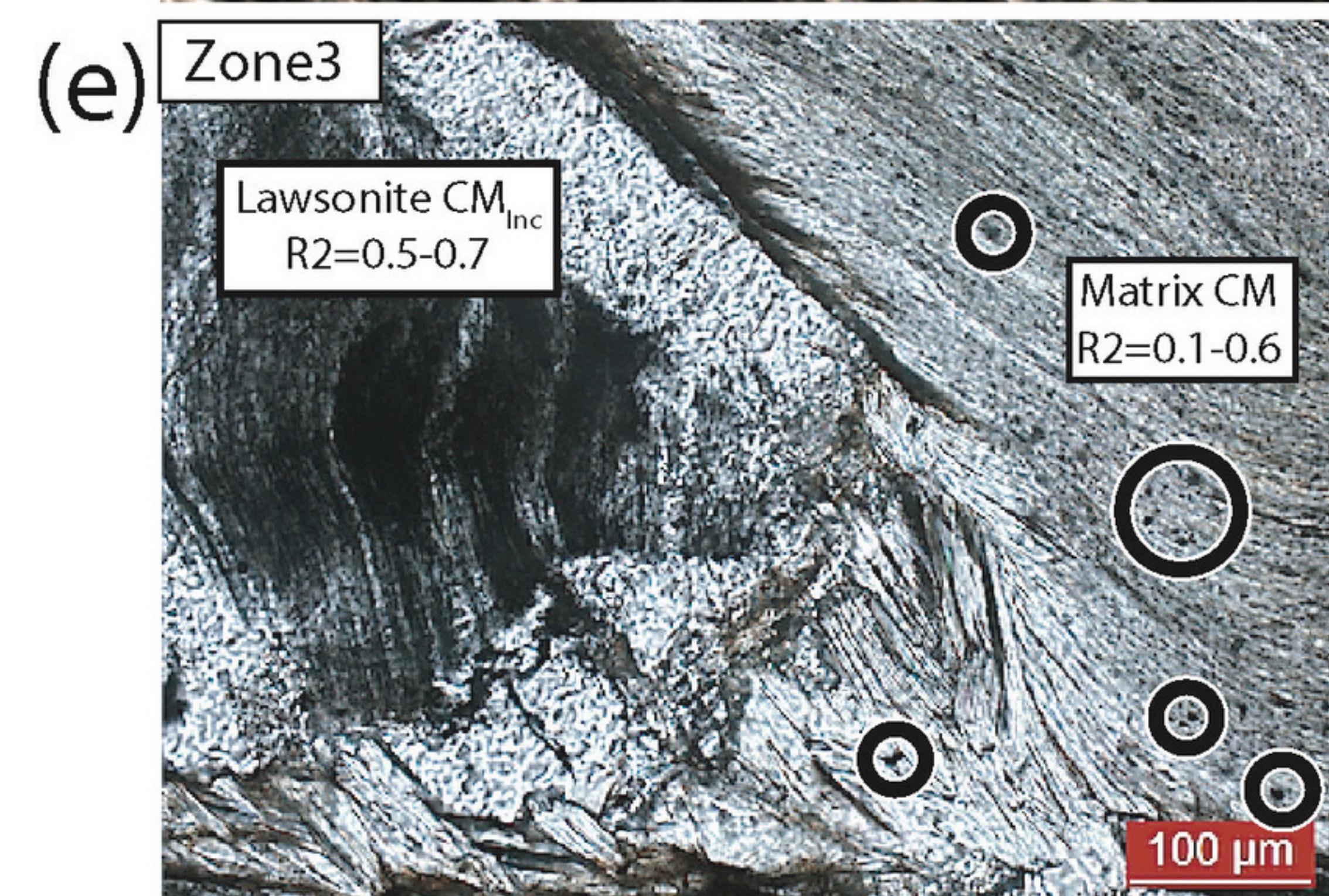
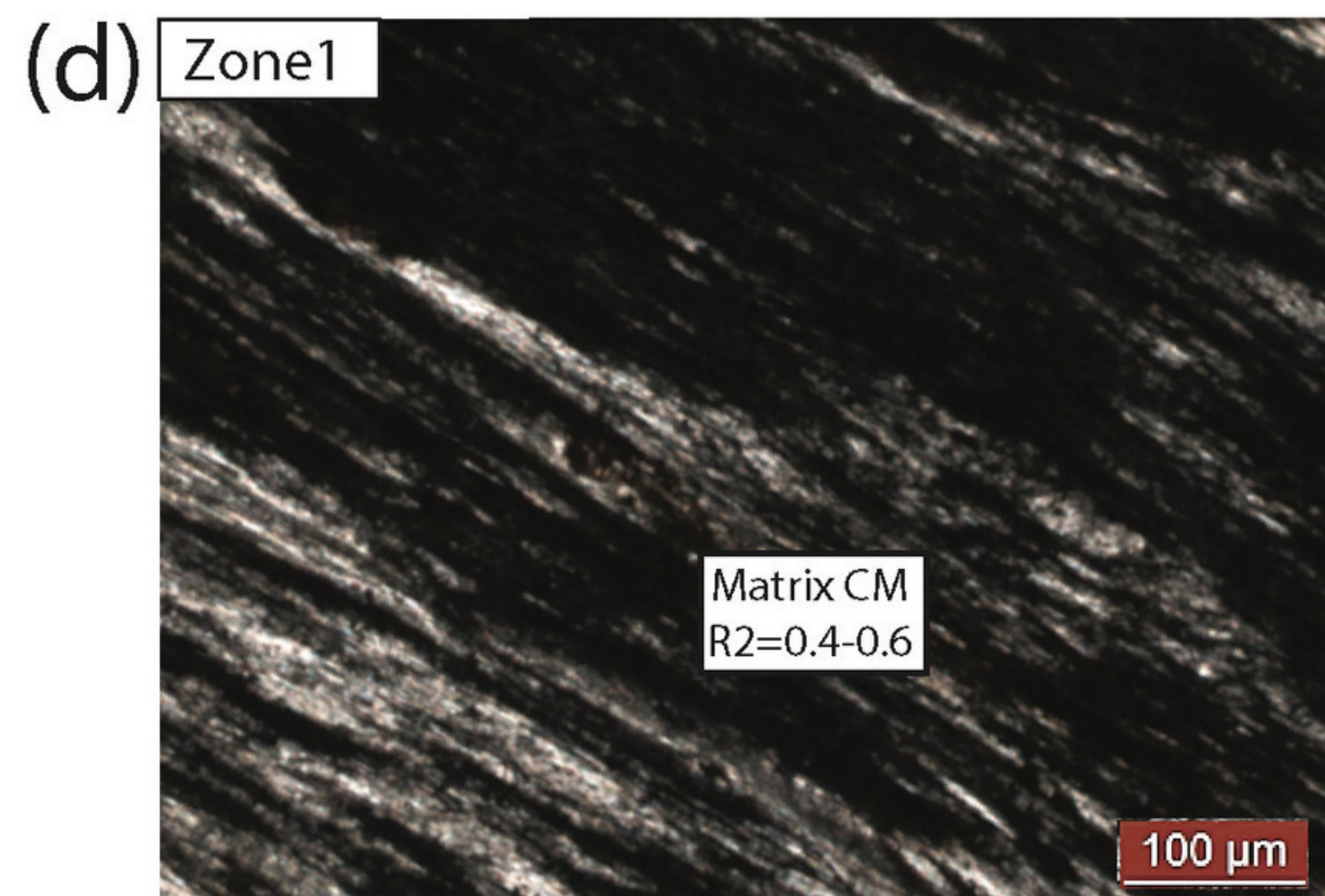
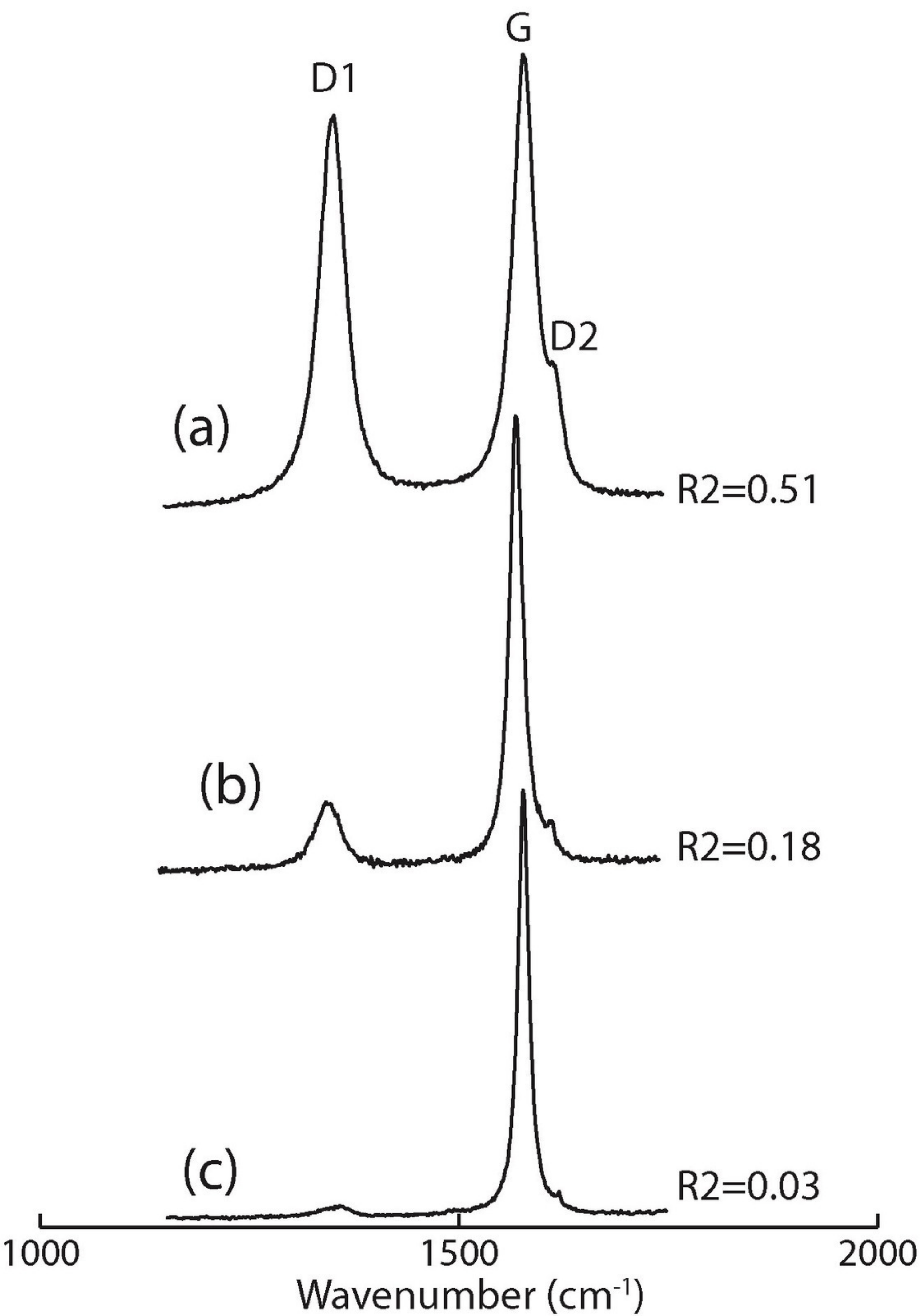
Alpine Corsica

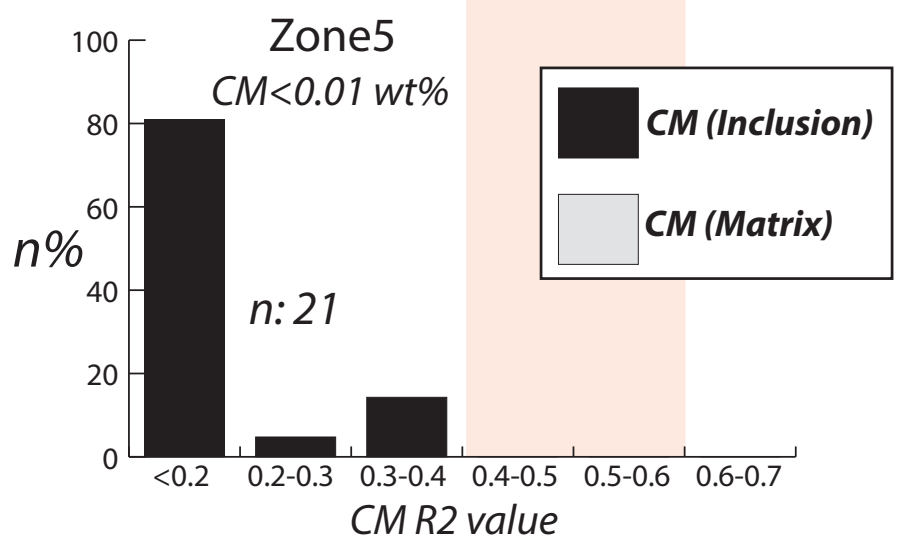
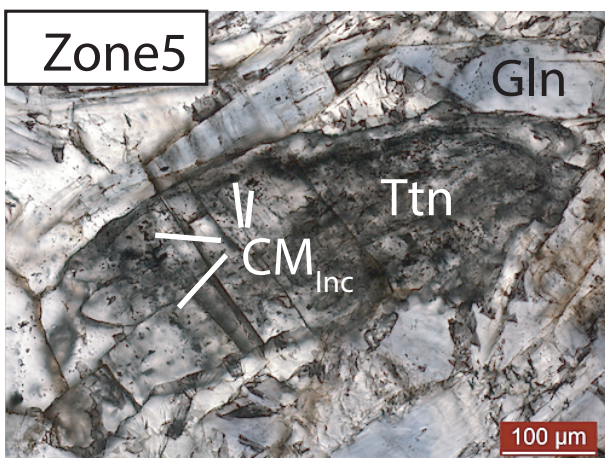
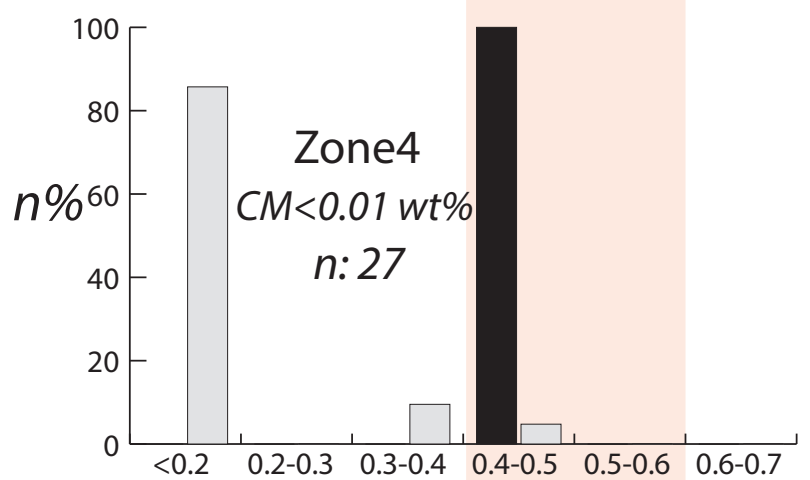
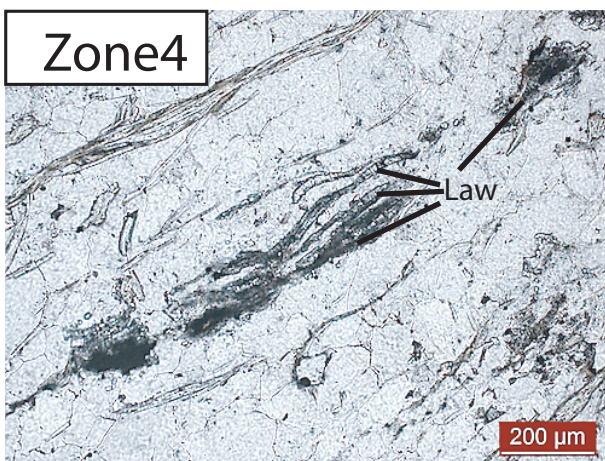
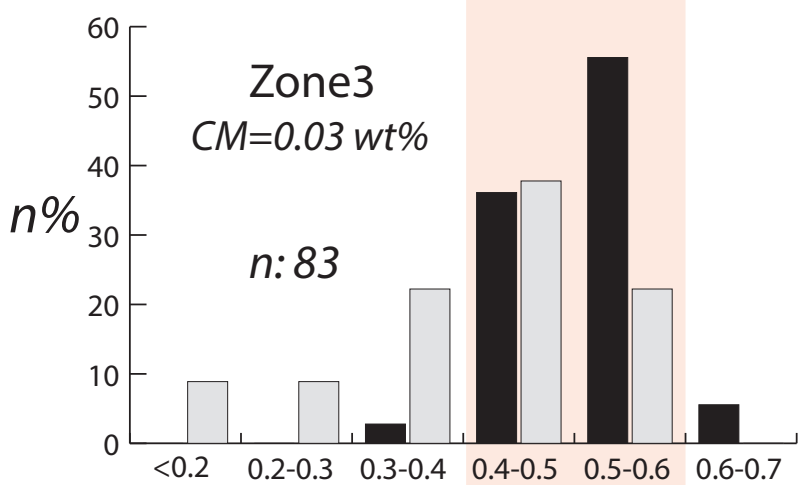
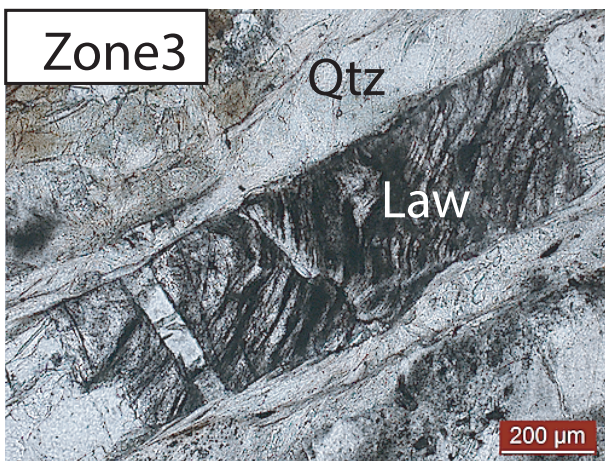
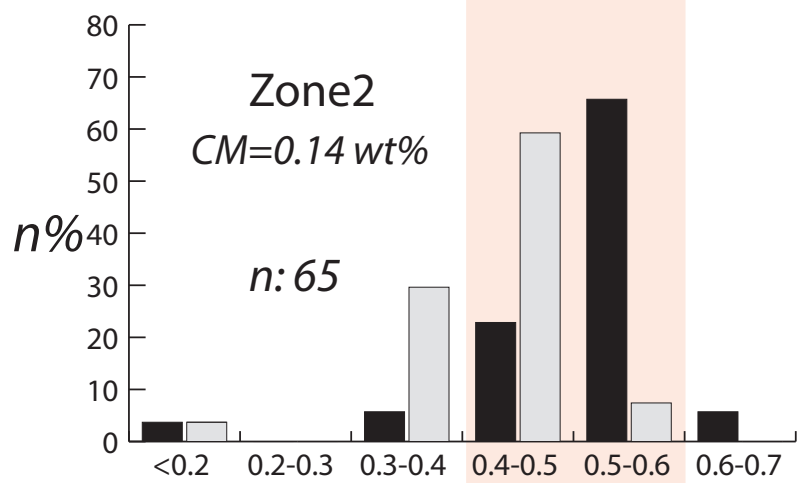
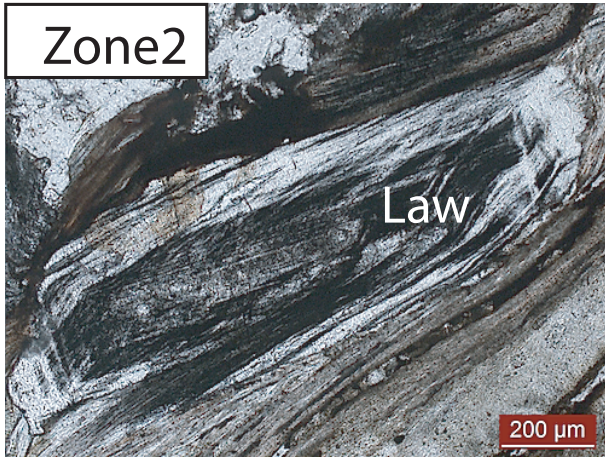
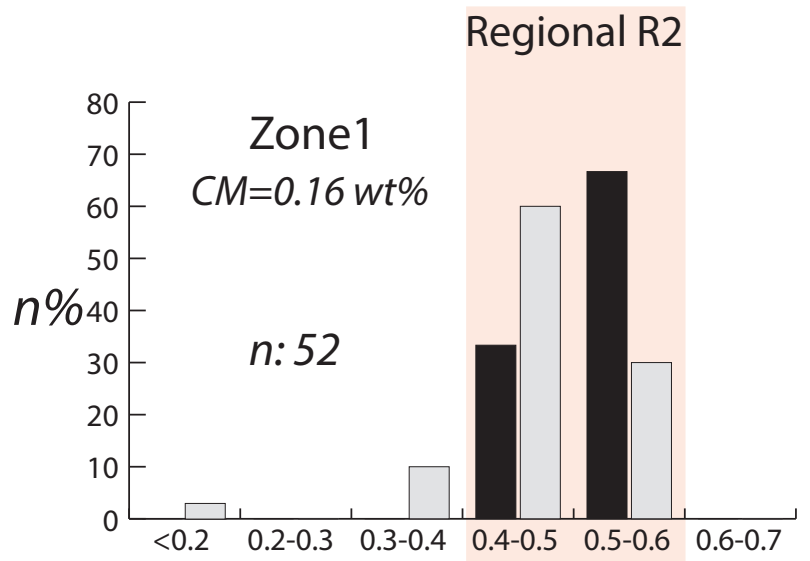
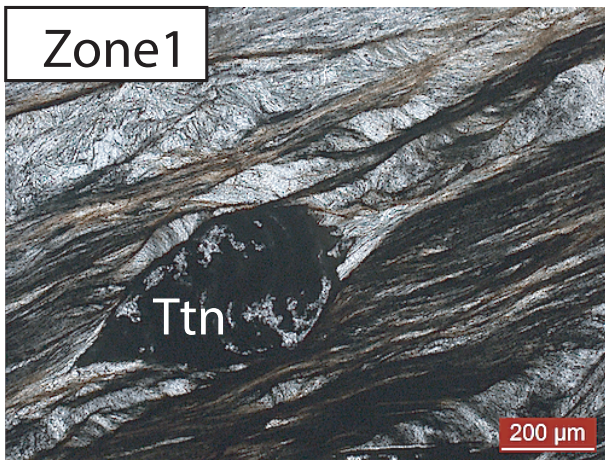
Western Alps

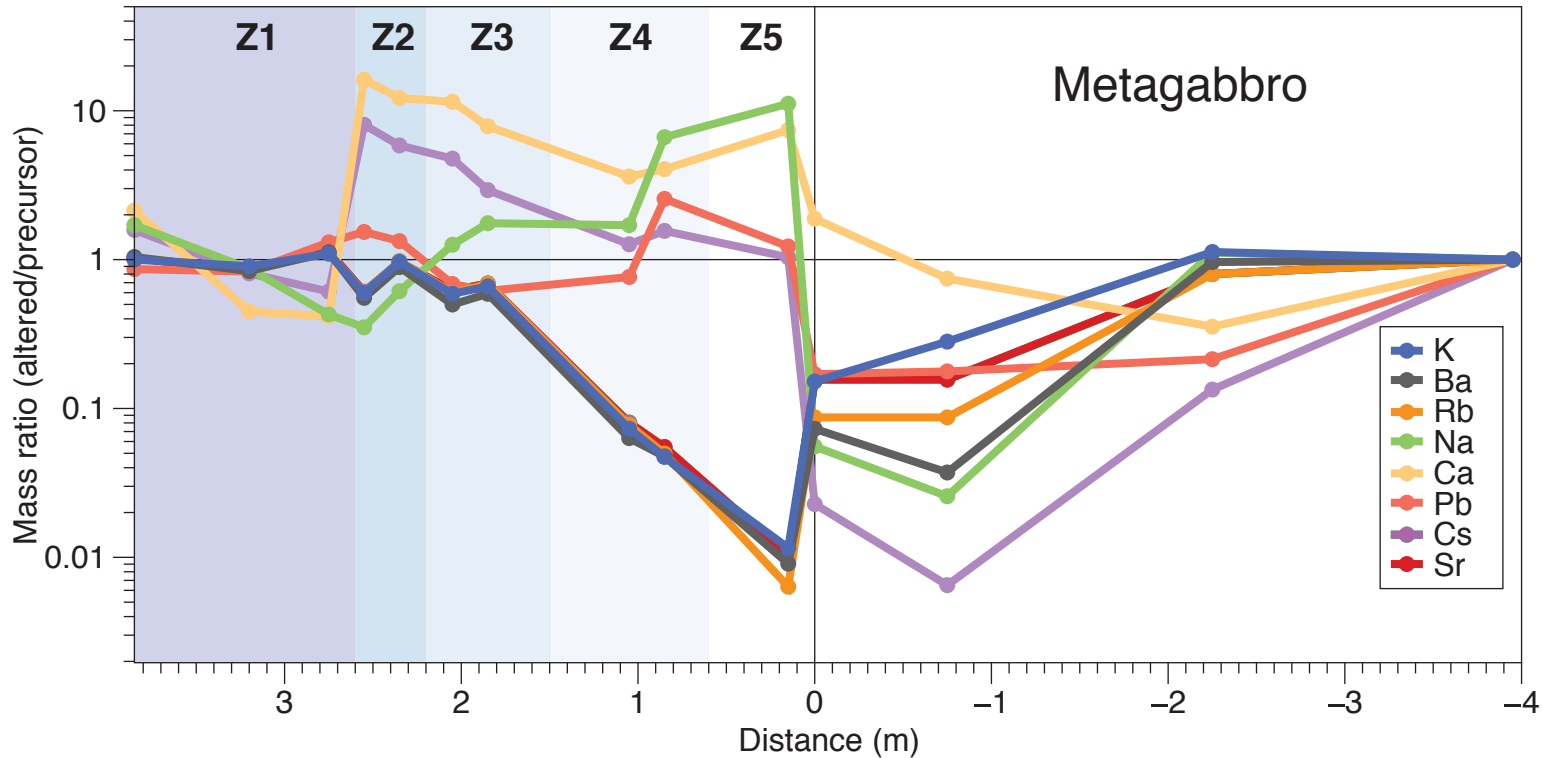


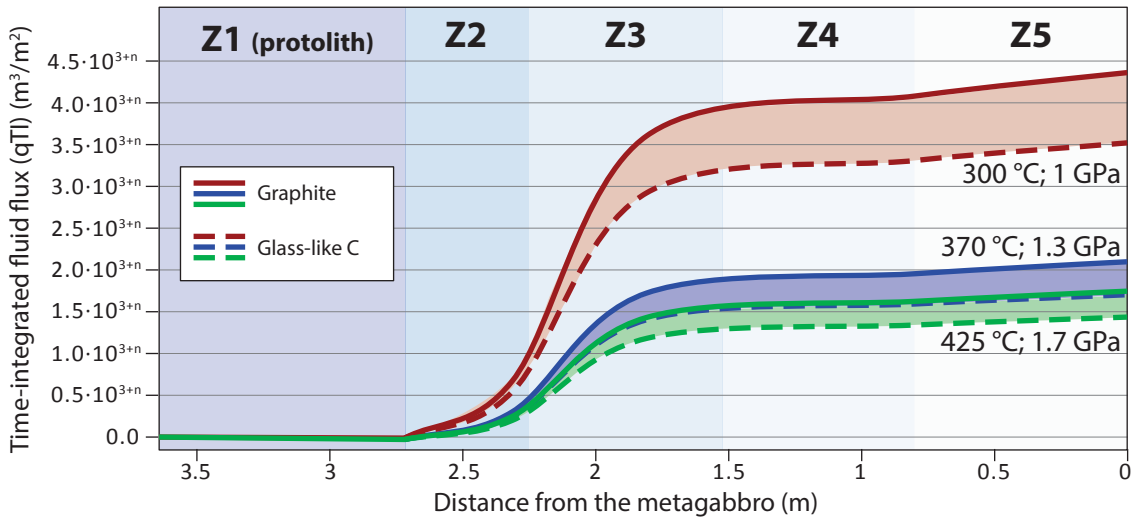












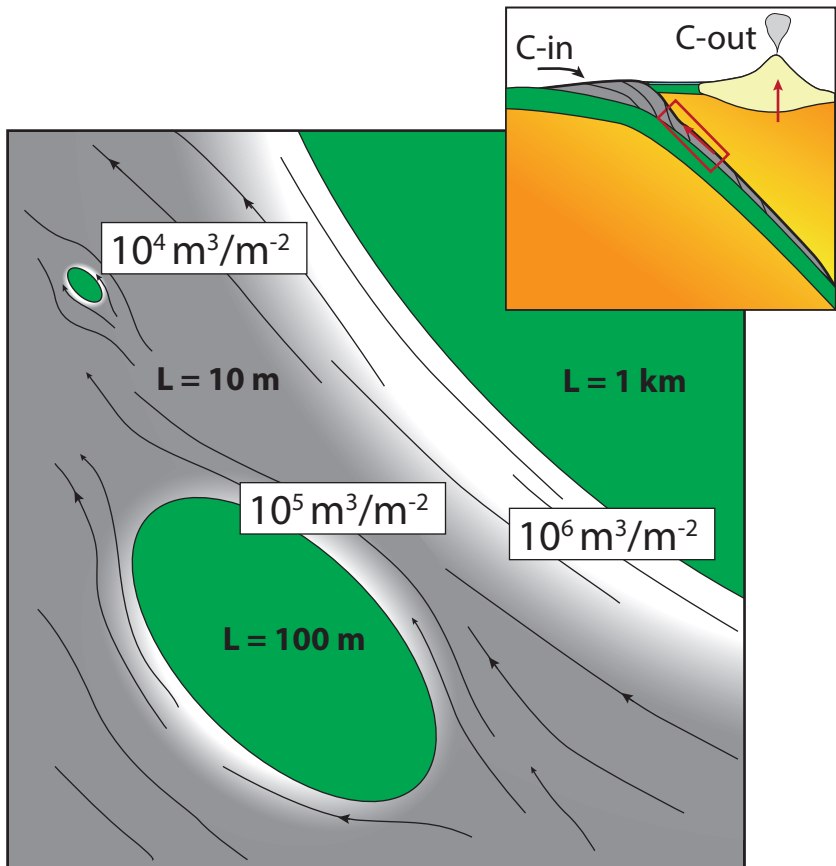


Table 1. Bulk organic C and total CO₂ content in the selected samples across the metasomatic aureole.

| Sample | Z1 | | | Z2 | | Z3 | | Z4 | | Z5 | Metagabbro | | | |
|------------------------|------|------|------|------|------|------|------|------|------|------|------------|------|------|------|
| | 12-4 | 2h | 2g | 2f | 2e | 2d | 2c | 23 | 2b | 24 | 25 | 28 | 2a | 29 |
| Corg (wt.%) | 0.13 | 0.13 | 0.16 | 0.1 | 0.14 | 0.02 | 0.03 | <DL | <DL | <DL | 0.01 | <DL | 0.01 | <DL |
| CO ₂ (wt.%) | 0.63 | 0.68 | 0.68 | 0.93 | 0.63 | 0.24 | 0.13 | 0.06 | 0.06 | 0.04 | 0.09 | 0.09 | 0.08 | 0.02 |

Table 2. RSCM R2 values of matrix and inclusion CM throughout the studied reaction zone.

| Zone1 | | Zone2 | | | | Zone3 | | | | Zone4 | | Zone5 |
|-----------|------|--------------------|-----------|-------------------------|------|-----------|-------------------------|------|-------------------------|-----------|-------------------------|--------------------|
| 2G matrix | | 2G inclusion (Ttn) | 2E matrix | 2E inclusion (Law, Ttn) | | 2D matrix | 2D inclusion (Law, Ttn) | | 2C inclusion (Law, Ttn) | 23 matrix | 23 inclusion (Law, Ttn) | 24 inclusion (Ttn) |
| 0.51 | 0.47 | 0.53 | 0.47 | 0.57 | 0.49 | 0.49 | 0.53 | 0.59 | 0.58 | 0.32 | 0.40 | 0.29 |
| 0.36 | 0.53 | 0.54 | 0.41 | 0.60 | 0.58 | 0.41 | 0.50 | 0.38 | 0.55 | 0.02 | 0.44 | 0.02 |
| 0.33 | 0.50 | 0.54 | 0.45 | 0.62 | 0.49 | 0.44 | 0.54 | 0.35 | 0.45 | 0.04 | 0.42 | 0.05 |
| 0.48 | 0.59 | 0.53 | 0.45 | 0.58 | 0.48 | 0.50 | 0.48 | 0.57 | 0.52 | 0.02 | 0.48 | 0.02 |
| 0.31 | 0.50 | 0.51 | 0.43 | 0.58 | 0.53 | 0.56 | 0.45 | 0.25 | 0.54 | 0.03 | 0.45 | 0.07 |
| 0.49 | 0.50 | 0.50 | 0.37 | 0.54 | 0.60 | 0.44 | 0.49 | 0.33 | 0.57 | 0.02 | 0.42 | 0.13 |
| 0.49 | 0.47 | 0.50 | 0.41 | 0.56 | 0.60 | 0.39 | 0.41 | 0.23 | 0.56 | 0.03 | | 0.17 |
| 0.48 | 0.45 | 0.50 | 0.39 | 0.57 | 0.54 | 0.46 | 0.44 | 0.34 | 0.57 | 0.05 | | 0.09 |
| 0.48 | 0.47 | 0.52 | 0.38 | 0.44 | | 0.53 | 0.50 | 0.09 | 0.52 | 0.03 | | 0.10 |
| 0.46 | 0.48 | 0.49 | 0.47 | 0.42 | | 0.52 | 0.56 | 0.11 | 0.56 | 0.10 | | 0.13 |
| 0.47 | 0.49 | 0.46 | 0.45 | 0.38 | | 0.40 | 0.44 | 0.15 | 0.59 | 0.06 | | 0.03 |
| 0.48 | 0.46 | 0.52 | 0.45 | 0.58 | | 0.57 | 0.39 | 0.54 | | 0.14 | | 0.32 |
| 0.49 | 0.54 | 0.58 | 0.43 | 0.59 | | 0.58 | 0.46 | 0.20 | | 0.00 | | 0.02 |
| 0.43 | 0.54 | | 0.36 | 0.62 | | 0.47 | 0.53 | 0.24 | | 0.15 | | 0.03 |
| 0.44 | 0.47 | | 0.41 | 0.58 | | 0.45 | 0.53 | 0.25 | | 0.01 | | 0.02 |
| 0.52 | 0.47 | | 0.39 | 0.58 | | 0.39 | 0.59 | 0.34 | | 0.39 | | 0.36 |
| 0.53 | 0.42 | | 0.38 | 0.55 | | 0.39 | 0.48 | 0.33 | | 0.45 | | 0.27 |
| 0.52 | 0.52 | | 0.42 | 0.56 | | 0.43 | 0.54 | | | 0.01 | | 0.35 |
| 0.51 | 0.47 | | 0.49 | 0.57 | | 0.54 | 0.54 | | | 0.07 | | 0.01 |
| 0.51 | 0.48 | | 0.30 | 0.44 | | 0.45 | 0.56 | | | 0.18 | | 0.05 |
| 0.49 | 0.49 | | 0.46 | 0.42 | | 0.38 | 0.48 | | | 0.18 | | 0.03 |
| 0.51 | 0.50 | | 0.47 | 0.41 | | 0.45 | 0.42 | | | | | 0.15 |
| 0.50 | 0.49 | | 0.16 | 0.38 | | 0.41 | 0.60 | | | | | |
| 0.52 | | | 0.50 | 0.58 | | 0.49 | 0.49 | | | | | |
| 0.38 | | | 0.50 | 0.14 | | 0.48 | 0.60 | | | | | |
| 0.07 | | | 0.48 | 0.58 | | 0.46 | 0.60 | | | | | |
| 0.50 | | | 0.49 | 0.59 | | 0.48 | | | | | | |
| 0.45 | | | 0.33 | 0.58 | | 0.55 | | | | | | |
| 0.34 | | | | 0.58 | | 0.44 | | | | | | |

Table 3. Calculated fractional mass change and organic C loss per 100g of rock for Zr, Hf, and Th.

| Sample | OC | Zr | | | Hf | | | Th | | |
|----------------|---------------|---------------|----------------------------|---------------------------|-------------|----------------------------|---------------------------|--------------|----------------------------|---------------------------|
| | | ppm | Fractional mass change (%) | Loss OC per 100g rock (g) | ppm | Fractional mass change (%) | Loss OC per 100g rock (g) | ppm | Fractional mass change (%) | Loss OC per 100g rock (g) |
| Zone1 | | | | | | | | | | |
| 2g | 0.160 | 122 | | | 3.4 | | | 13.04 | | |
| 2h | 0.130 | 108.3 | | | 3 | | | 10.09 | | |
| 12-4 | 0.130 | 164 | | | 4.4 | | | 15 | | |
| <i>Average</i> | <i>0.140</i> | <i>131.43</i> | | | <i>3.60</i> | | | <i>12.71</i> | | |
| <i>SD</i> | <i>0.017</i> | <i>29.02</i> | | | <i>0.72</i> | | | <i>2.47</i> | | |
| Zone2 | | | | | | | | | | |
| 2e | 0.140 | 146 | 11 | 0.02 | 4.1 | 14 | 0.02 | 13.79 | 8 | 0.01 |
| 2f | 0.100 | 105 | -43 | -0.06 | 2.9 | -42 | -0.06 | 10.7 | -40 | -0.06 |
| <i>Average</i> | <i>0.120</i> | <i>125.50</i> | <i>-16</i> | <i>-0.02</i> | <i>3.50</i> | <i>-14</i> | <i>-0.02</i> | <i>12.25</i> | <i>-16</i> | <i>-0.02</i> |
| <i>SD</i> | <i>0.028</i> | <i>28.99</i> | <i>38.20</i> | <i>0.05</i> | <i>0.85</i> | <i>40</i> | <i>0.06</i> | <i>2.18</i> | <i>34</i> | <i>0.05</i> |
| Zone3 | | | | | | | | | | |
| 2c | 0.030 | 133 | -78 | -0.11 | 3.5 | -79 | -0.11 | 11.14 | -81 | -0.11 |
| 2d | 0.020 | 102.2 | -89 | -0.12 | 2.8 | -89 | -0.12 | 9.887 | -89 | -0.12 |
| <i>Average</i> | <i>0.025</i> | <i>117.60</i> | <i>-84</i> | <i>-0.12</i> | <i>3.15</i> | <i>-84</i> | <i>-0.12</i> | <i>10.51</i> | <i>-85</i> | <i>-0.12</i> |
| <i>SD</i> | <i>0.007</i> | <i>21.78</i> | <i>7.48</i> | <i>0.01</i> | <i>0.49</i> | <i>7</i> | <i>0.01</i> | <i>0.89</i> | <i>5</i> | <i>0.01</i> |
| Zone4 | | | | | | | | | | |
| 2b | 0.004* | 239 | -95 | -0.13 | 5.9 | -95 | -0.13 | 4.639 | -99 | -0.14 |
| 23 | 0.004* | 288.1 | -94 | -0.13 | 7.2 | -94 | -0.13 | 9.798 | -98 | -0.14 |
| <i>Average</i> | <i>0.004*</i> | <i>263.55</i> | <i>-94.27</i> | <i>-0.13</i> | <i>6.55</i> | <i>-95</i> | <i>-0.13</i> | <i>7.22</i> | <i>-98</i> | <i>-0.14</i> |
| <i>SD</i> | | <i>34.72</i> | <i>0.75</i> | <i>0.00</i> | <i>0.92</i> | <i>1</i> | <i>0.00</i> | <i>3.65</i> | <i>1</i> | <i>0.00</i> |
| Zone5 | | | | | | | | | | |
| 24 | 0* | 181.7 | -100 | -0.14 | 3.6 | -100 | -0.14 | 15.12 | -100 | -0.14 |

* <Detection limit (<0.01 wt.%); values calculated based on the proportions of disordered (R2>0.2) and graphitic (R2<0.2) CM.

Table 4. Fluid component speciation considered for mass balances and flux estimates, calculated by thermodynamic modelling of COH fluids saturated with graphite and glass-like carbon

| | Buffer | P (GPa) | T (°C) | H₂O | CH₄ | CO₂ | X_C | molC/molH₂O |
|---------------------|----------------------|----------------|---------------|-----------------------|-----------------------|-----------------------|----------------------|-------------------------------|
| Graphite | H ₂ O max | 1 | 300 | 0.99985 | 1.18E-04 | 3.55E-05 | 1.53E-04 | 1.53E-04 |
| Glass-like C | H ₂ O max | 1 | 300 | 0.99981 | 1.45E-04 | 4.37E-05 | 1.89E-04 | 1.89E-04 |
| Graphite | H ₂ O max | 1.3 | 370 | 0.99968 | 2.18E-04 | 9.99E-05 | 3.18E-04 | 3.18E-04 |
| Glass-like C | H ₂ O max | 1.3 | 370 | 0.99962 | 2.61E-04 | 1.20E-04 | 3.81E-04 | 3.82E-04 |
| Graphite | H ₂ O max | 1.7 | 425 | 0.99961 | 2.55E-04 | 1.33E-04 | 3.89E-04 | 3.89E-04 |
| Glass-like C | H ₂ O max | 1.7 | 425 | 0.99954 | 3.02E-04 | 1.58E-04 | 4.59E-04 | 4.59E-04 |

Table 5. Calculated time-integrated fluid fluxes at H₂O-maximum. For each sample, qTI is calculated by considering the CM fractional change relative to the average of Z1.

| Zone | Sample | L (m) | 300 °C, 1.0 GPa | | 370 °C, 1.3 GPa | | 425 °C, 1.7 GPa | | Zone | Sample | L (m) | 300 °C, 1.0 GPa | | 370 °C, 1.3 GPa | | 425 °C, 1.7 GPa | | |
|-------|--------|-------|-----------------|--------------|-----------------|--------------|-----------------|--------------|-------|--------|-----------|-----------------|--------------|-----------------|--------------|-----------------|--------------|-----------|
| | | | qTI | | qTI | | qTI | | | | | qTI | | qTI | | qTI | | |
| | | | Graphite | Glass-like C | Graphite | Glass-like C | Graphite | Glass-like C | | | | Graphite | Glass-like C | Graphite | Glass-like C | Graphite | Glass-like C | |
| Zone1 | 12-4 | 1 | 6.93E+02 | 5.63E+02 | 3.34E+02 | 2.78E+02 | 2.73E+02 | 2.31E+02 | Zone3 | 2d | 1 | -3.86E+03 | -3.13E+03 | -1.86E+03 | -1.55E+03 | -1.52E+03 | -1.29E+03 | |
| | | 10 | 6.93E+03 | 5.63E+03 | 3.34E+03 | 2.78E+03 | 2.73E+03 | 2.31E+03 | | | 10 | -3.86E+04 | -3.13E+04 | -1.86E+04 | -1.55E+04 | -1.52E+04 | -1.29E+04 | |
| | | 100 | 6.93E+04 | 5.63E+04 | 3.34E+04 | 2.78E+04 | 2.73E+04 | 2.31E+04 | | | 100 | -3.86E+05 | -3.13E+05 | -1.86E+05 | -1.55E+05 | -1.52E+05 | -1.29E+05 | |
| | | 1000 | 6.93E+05 | 5.63E+05 | 3.34E+05 | 2.78E+05 | 2.73E+05 | 2.31E+05 | | | 1000 | -3.86E+06 | -3.13E+06 | -1.86E+06 | -1.55E+06 | -1.52E+06 | -1.29E+06 | |
| | 2h | 1 | -9.96E+02 | -8.10E+02 | -4.81E+02 | -4.00E+02 | -3.93E+02 | -3.32E+02 | | 2c | 1 | -3.38E+03 | -2.75E+03 | -1.63E+03 | -1.36E+03 | -1.33E+03 | -1.13E+03 | |
| | | 10 | -9.96E+03 | -8.10E+03 | -4.81E+03 | -4.00E+03 | -3.93E+03 | -3.32E+03 | | | 10 | -3.38E+04 | -2.75E+04 | -1.63E+04 | -1.36E+04 | -1.33E+04 | -1.13E+04 | |
| | | 100 | -9.96E+04 | -8.10E+04 | -4.81E+04 | -4.00E+04 | -3.93E+04 | -3.32E+04 | | | 100 | -3.38E+05 | -2.75E+05 | -1.63E+05 | -1.36E+05 | -1.33E+05 | -1.13E+05 | |
| | | 1000 | -9.96E+05 | -8.10E+05 | -4.81E+05 | -4.00E+05 | -3.93E+05 | -3.32E+05 | | | 1000 | -3.38E+06 | -2.75E+06 | -1.63E+06 | -1.36E+06 | -1.33E+06 | -1.13E+06 | |
| | 2g | 1 | 1.25E+02 | 1.04E+02 | 2.60E+02 | 2.11E+02 | 1.02E+02 | 8.67E+01 | | Zone4 | 2b | 1 | -4.12E+03 | -3.34E+03 | -1.99E+03 | -1.65E+03 | -1.62E+03 | -1.37E+03 |
| | | 10 | 1.25E+03 | 1.04E+03 | 2.60E+03 | 2.11E+03 | 1.02E+03 | 8.67E+02 | | | | 10 | -4.12E+04 | -3.34E+04 | -1.99E+04 | -1.65E+04 | -1.62E+04 | -1.37E+04 |
| | | 100 | 1.25E+04 | 1.04E+04 | 2.60E+04 | 2.11E+04 | 1.02E+04 | 8.67E+03 | | | | 100 | -4.12E+05 | -3.34E+05 | -1.99E+05 | -1.65E+05 | -1.62E+05 | -1.37E+05 |
| | | 1000 | 1.25E+05 | 1.04E+05 | 2.60E+05 | 2.11E+05 | 1.02E+05 | 8.67E+04 | | | | 1000 | -4.12E+06 | -3.34E+06 | -1.99E+06 | -1.65E+06 | -1.62E+06 | -1.37E+06 |
| Zone2 | 2f | 1 | -1.86E+03 | -1.51E+03 | -8.99E+02 | -7.48E+02 | -7.34E+02 | -6.21E+02 | 23 | 1 | -4.07E+03 | -3.31E+03 | -1.96E+03 | -1.64E+03 | -1.60E+03 | -1.36E+03 | | |
| | | 10 | -1.86E+04 | -1.51E+04 | -8.99E+03 | -7.48E+03 | -7.34E+03 | -6.21E+03 | | 10 | -4.07E+04 | -3.31E+04 | -1.96E+04 | -1.64E+04 | -1.60E+04 | -1.36E+04 | | |
| | | 100 | -1.86E+05 | -1.51E+05 | -8.99E+04 | -7.48E+04 | -7.34E+04 | -6.21E+04 | | 100 | -4.07E+05 | -3.31E+05 | -1.96E+05 | -1.64E+05 | -1.60E+05 | -1.36E+05 | | |
| | | 1000 | -1.86E+06 | -1.51E+06 | -8.99E+05 | -7.48E+05 | -7.34E+05 | -6.21E+05 | | 1000 | -4.07E+06 | -3.31E+06 | -1.96E+06 | -1.64E+06 | -1.60E+06 | -1.36E+06 | | |
| | 2e | 1 | 4.77E+02 | 3.87E+02 | 2.30E+02 | 1.91E+02 | 1.88E+02 | 1.59E+02 | Zone5 | 24 | 1 | -4.33E+03 | -3.52E+03 | -2.09E+03 | -1.74E+03 | -1.71E+03 | -1.45E+03 | |
| | | 10 | 4.77E+03 | 3.87E+03 | 2.30E+03 | 1.91E+03 | 1.88E+03 | 1.59E+03 | | | 10 | -4.33E+04 | -3.52E+04 | -2.09E+04 | -1.74E+04 | -1.71E+04 | -1.45E+04 | |
| | | 100 | 4.77E+04 | 3.87E+04 | 2.30E+04 | 1.91E+04 | 1.88E+04 | 1.59E+04 | | | 100 | -4.33E+05 | -3.52E+05 | -2.09E+05 | -1.74E+05 | -1.71E+05 | -1.45E+05 | |
| | | 1000 | 4.77E+05 | 3.87E+05 | 2.30E+05 | 1.91E+05 | 1.88E+05 | 1.59E+05 | | | 1000 | -4.33E+06 | -3.52E+06 | -2.09E+06 | -1.74E+06 | -1.71E+06 | -1.45E+06 | |